doi:10.20944/preprints202208.0270.v1

Article

Numerical Simulation of Unsteady Flow Field around Monopile under the Combined Influence of Wave and Vibration

Yuxuan Shi [1,2], Yongzhou Cheng [1,2*] and Xiaoyun Huang [1,2]

[1] School of Hydraulic and Environmental Engineering, Changsha University of Science & Technology, Changsha 410114,Chi
[2] Key Laboratory of Water-Sediment Sciences and Water Disaster Prevention of Hunan Province, Changsha 410114,China; chengyz@csust.edu.cn
* Correspondence: chengyongzhou@163.com; Tel.: +86-1378-619-1344 (F.L.)

Abstract: The unsteady flow around the monopile under the influence of wave and vibration is studied by numerical method. Based on VOF model and SST Turbulence model, combined with Intermittent Transition model and dynamic mesh method, wave generation and pile vibration in numerical flume are simulated. The flow field around vibrating monopile in a calm water flume and a wave flume is simulated and the simulation results are compared. The calculation results show that the monopile vibration has a great disturbance to the unsteady flow around the pile, and the disturbance degree intensifies with the increase of the vibration amplitude of the monopile: Under the action of inertia, the vibration of the monopile leads to the reattachment of the shedding vortices; Under the influence of the reattachment vortices, the asymmetry of the vorticity on the side wall of the monopile intensifies; The intensification of the disturbance causes the reduction of the phase lead angle of the bed shear stress on the side of the single pile, and an additional high bed shear stress appears on the side of the monopile. In addition, the vortex structure formed alternately around the monopile during the vibration process leads to the periodic change of the high bed shear stress.

Keywords: Two-phase flow; Turbulence model; Disturbance; Vortex field; Bed shear stress

0. Introduction

Offshore wind turbines have been extensively utilized because of the development of renewable energy [1,2]. Monopile is a crucial foundation type of offshore wind turbines. In the working environment of the turbine, monopiles are commonly subjected to the operating load of the top motor, as well as complex wind, wave, and current loads, which are often periodic and long-term [3]. Under the influence of such periodic loads, long-term cyclic horizontal displacement is produced in monopiles. This horizontal displacement causes the oscillation of the water body around the pile. Combined with the existing wind, wave, and current, which results in a complex impact on the flow pattern around the pile, and then affects the scouring around the pile. Therefore, it is necessary to further examine the unsteady flow field adjacent to the pile under the combined action of waves and vibrations.

For the unsteady flow field nearby the pile, the vortices around the pile have attracted much attention. When the pile moves in the pulse, inertia plays a supporting role in the shedding of the primary vortices, and the phenomenon of vortices reattachment caused by the change of velocity pulse is detectable [4–6]. For the vortex fields around the pile in the wave flume under the action of wave loading, compared with the general flow around a cylinder, the vortex structure shows apparent differences: the horseshoe vortices emerges only during a certain portion of the half period of the wave downwelling with a significantly diminished "strength", and the Lee-wake flow pattern presents multiple vortices shedding regimes governed by the Keulegan-Carpenter number [7]. In the present

doi:10.20944/preprints202208.0270.v1

scrutiny, the influence of the pile vibration on the vortex fields is of high interest since making them more complex.

Under the influence of wave and vibration, the velocity distribution near the wall dramatically varies, and the effects of the shear flow and eddy current become very noticeable. The resulting changes in the bed shear stress are also of great concern. The vortex structure in the flow field leads to the increase of the velocity gradient near the wall[8,9], which affects the time history of the oscillating flow with periodic changes, and leads to the occurrence of the peak shear stress[10–12]. The increase of shear stress caused by the horseshoe vortices are also the main driving force, leading to the scouring around the pile[13–15]. Additionally, the change of the overall shear stress caused by the variation of the pile side accelerated flow and wake vortices, forming a high shear stress region[16]. The external oscillating flow penetrates the boundary layer, which may also lead to the growth of the bed shear stress[17].

Another noteworthy phenomenon is that under the influence of the phase discrepancy between the free stream velocity and the boundary layer one, there is a phase lead effect in the bed shear stress time history. Van der[18] conducted experiments in an oscillating flow tunnel with rough walls to explore the influence of acceleration skewness on sediment transport in oscillating flows. This study considers that the phase leading angle changes exponentially with the maximum velocity of the oscillating flow, and the leading angle of the onshore half cycle is greater than the offshore half cycle. However, through the conclusion of the wave flume experiment, Xie[19] pointed out that Van der's data did not support the law of exponential change, and there was no definite comparison relationship between the leading angles of the shore half cycle and the offshore half cycle.

To summarize, the vortex fields and shear flow around the pile are the key factors to characterize the flow regime around the pile. The previous research works on the local flow field around the pile wave flume are mostly based on the pile under static conditions, while the case of the pile under the combined action of wave and vibration is often simplified to a certain extent, and there is still a lack of detailed analysis and systematic research[20]. Therefore, it is of particular scientific significance to examine the unsteady flow around the pile under the combined action of waves and vibrations.

In the current work, in order to explore the influence of the pile vibration amplitude on the flow field around the monopile in the calm water flume and the wave flume, the changes in vibration vortex fields and shear stress in the calm water flume, and the changes of vibration vortex fields and shear stress in the wave flume are carefully simulated and compared. By this view, Sections 1 and 2 introduce the numerical model employed and the simulated cases in the simulation. Section 3 aims to verify the effectiveness of the numerical model. In Section 4, the development of the vortex fields and the change of the bed shear stress are taken as the research objects, and the simulation results for the static water flume(in Section 4.2) and wave flume(in Section 4.3) are displayed, compared and discussed. Finally, the simulation results are summarized in Section 5.

1. Numerical model

1.1. Governing equations

In this study, VOF model and SST model are used to simulate the flow pattern in numerical flume. This coupling model has good effects on the simulation of waves and the flow field around the cylindrical pile[21–23]. The following equations are mainly solved:

$$\begin{aligned}
&\frac{1}{\rho_q}\left[\frac{\partial}{\partial t}(\alpha_q\rho_q)+\nabla\cdot(\alpha_q\rho_q\vec{v}_q)\right]=\frac{1}{\rho_q}\left[S_{\alpha_q}+\sum_{p=1}^{n}(m_{pq}-m_{qp})\right]\\
&\frac{\partial}{\partial t}(\rho\vec{v})+\nabla\cdot(\rho\vec{v}\vec{v})=-\nabla p+\nabla\cdot\left[\mu\left(\nabla\vec{v}+\nabla\vec{v}^{T}\right)\right]+\rho\vec{g}+\vec{F}\\
&\frac{\partial}{\partial t}(\rho k)+\frac{\partial}{\partial x_i}(\rho k u_i)=\frac{\partial}{\partial x_j}\left(\Gamma_k\frac{\partial k}{\partial x_j}\right)+G_k+S_k-Y_k\\
&\frac{\partial}{\partial t}(\rho\omega)+\frac{\partial}{\partial x_j}(\rho\omega u_j)=\frac{\partial}{\partial x_j}\left(\Gamma_\omega\frac{\partial\omega}{\partial x_j}\right)+G_\omega+D_\omega+S_\omega-Y_\omega
\end{aligned}\tag{1}$$

The first two equations are volume fraction equation (continuity equation in VOF model) and momentum equation, and the last two are turbulence equations.

In each control volume, the volume fractions of all phases sum to unity. The fields for all variables and properties are shared by the phases and represent volume averaged values, as long as the volume fraction of each of the phases is known at each location.

$\alpha_q = 0$, The cell is empty of the q fluid;

$\alpha_q = 1$, The cell is full of the q fluid;

$0 < \alpha_q < 1$, The cell contains the interface between the q fluid and one or more other fluids. Substitute this fraction into the continuity equation:

$$\rho_q \left[\frac{\partial}{\partial t}(\alpha_q \rho_q) + \nabla \cdot (\alpha_q \rho_q \vec{v}_q) \right] = \frac{1}{\rho_q} \left[S_{\alpha_q} + \sum_{p=1}^{n} (m_{pq} - m_{qp}) \right] \tag{2}$$

The equation is the deformation of the continuous equation under the VOF model, where m is the mass transfer between phase p and phase q, S is the source term(This term is 0 in this study).

Based on the above phase properties, solve the momentum equation of multiphase flow:

$$\frac{\partial}{\partial t}(\rho \vec{v}) + \nabla \cdot (\rho \vec{v} \vec{v}) = -\nabla p + \nabla \cdot \left[\mu \left(\nabla \vec{v} + \nabla \vec{v}^T \right) \right] + \rho \vec{g} + \vec{F} \tag{3}$$

It is worth noting that only one momentum equation is solved, and the phase velocity obtained is shared by all phases.

In most hydrodynamic problems, gravity or other inertial forces dominate, so the effect of surface tension is almost negligible. The critical dimensionless parameter (Weber number) is usually used to characterize the effect of surface tension. The Weber number in this study is 2505 (Stokes wave), which shows that the influence of inertia force is much greater than that of surface tension. Therefore, in this study, the effect of surface tension is very small and is almost negligible.

The SST model includes all the refinements of the BSL model, and in addition accounts for the transport of the turbulence shear stress in the definition of the turbulent viscosity.

Where k is turbulence kinetic energy, ω is specific turbulence dissipation rate. Γ_k and Γ_ω represent the effective diffusivity of k and ω [24]:

$$\begin{aligned} \Gamma_k &= \mu + \mu_t \tfrac{1}{\sigma_k} \\ \Gamma_\omega &= \mu + \mu_t \tfrac{1}{\sigma_\omega} \end{aligned} \tag{4}$$

The characteristic of SST model differ from other $k - \omega$ model is the consideration of the transport of the turbulent shear stress:

$$\begin{aligned} \mu_t &= \frac{\rho k}{\omega} \frac{1}{\max\left[\frac{1}{\alpha^*}, \frac{S F_2}{\alpha_1 \omega}\right]} \\ F_2 &= \tanh\left(\phi_2^2\right) \\ \phi_2 &= \max\left[2 \frac{\sqrt{k}}{0.09 \omega y}, \frac{500 \mu}{\rho y^2 \omega}\right] \end{aligned} \tag{5}$$

F_2 is used to manipulate the next surface condition. In ϕ_2 , y is the distance to the next surface.

F_1 function is worth noting. F_1 is a hyperbolic tangent function, and its variation trend with parameter is as follows:

$$\begin{aligned} F_1 &= \tanh\left(\arg_1^4\right) \\ \arg_1 &= \min\left[\max\left(\frac{\sqrt{k}}{0.09 \omega y}, \frac{500 \mu}{\rho y^2 \omega}\right), \frac{4 \rho k}{\sigma_{\omega,2} D_\omega^+ y^2}\right] \\ D_\omega^+ &= \max\left[2 \rho \frac{1}{\sigma_{\omega,2}} \frac{1}{\omega} \frac{\partial k}{\partial x_j} \frac{\partial \omega}{\partial x_j}, 10^{-10}\right] \end{aligned} \tag{6}$$

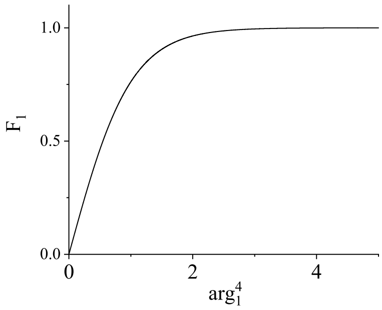

Figure 1. F_1 function.

As F_1 tends to 1, the model is $k-\epsilon$ model; As $F_1 = 0$, the model is $k-\omega$ model. Therefore, SST model has the characteristics of $k-\epsilon$and $k-\omega$ model. When the near wall grid is dense, the near wall flow field would be directly solved by the $k-\omega$ model, and the $k-\epsilon$ model used to calculate the near wall flow field when the grid is sparse.

G represents the production of k and ω , D represents cross-diffusion term of k and ω.

1.2. Intermittency transition model

In this study, in order to deal with standard bypass transition and shedding conditions, the γ(intermittency) transition model is used[25].

Transport equation of intermittency transition model:

$$\frac{\partial(\rho\gamma)}{\partial t}+\frac{\partial(\rho U_j\gamma)}{\partial x_j}=P_\gamma-E_\gamma+\frac{\partial}{\partial x_j}\left[\left(\mu+\frac{\mu_t}{\sigma_\gamma}\right)\frac{\partial\gamma}{\partial x_j}\right] \tag{7}$$

The two source terms on the right of the equation are transition source and destruction/relaminarization source:

$$\begin{aligned}P_\gamma &= F_{\text{length}}\,\rho S_\gamma(1-\gamma)F_{\text{onset}}\\ E_\gamma &= c_{a2}\rho\Omega\gamma F_{\text{turb}}\,(c_{e2}\gamma-1)\end{aligned} \tag{8}$$

F_{onset} represents transition onset which calculated by the following formulas:

$$\begin{aligned}&F_{\text{onset }1}=\frac{\mathrm{Re}_v}{2.2\,\mathrm{Re}_{\theta_c}},F_{\text{onset }2}=\min(2.0,F_{\text{onset1}}),\\ &F_{\text{onset }3}=\max\left(1-\left(\frac{R_T}{3.5}\right)^3,0\right),\\ &F_{\text{onset}}=\max(F_{\text{onset }2}-F_{\text{onset }3},0)\\ &F_{turb}=e-\left(\frac{R_T}{2}\right)^4\\ &R_T=\frac{\rho k}{\mu\omega}\\ &\mathrm{Re}_V=\frac{\rho d_w^2 S}{\mu}\\ &\mathrm{Re}_{\theta c}=f(T_{uL},\lambda_{\theta L})\end{aligned} \tag{9}$$

S represents the strain rate magnitude, Ω is the magnitude of the absolute vorticity rate, F_length is the length of transition zone, $C_{\alpha 2}$=0.06, C_{e2}=50.

1.3. Wave absorbing model

In order to prevent the reflection wave from affecting the wave making waveform, the damping source term wave elimination method is used to absorb it. The artificial viscous wave elimination is insensitive to the frequency (or wavelength) of the wave, and can effectively eliminate the waves of various frequencies (or wavelengths).

In this study, the damping source term is set in the wave absorbing region:

$$S = -f(x)\left[C_1\rho V + \frac{1}{2}C_2\rho|V|V\right] \tag{10}$$

In order to completely eliminate wave energy in the attenuation band and not cause the reflected wave as soon as it enters the attenuation band, the viscous drag coefficient must not be too minute or too large. Therefore, the viscous drag coefficient according to the law of quadratic function.

$$f(x) = \left(\frac{x - x_s}{x_e - x_s}\right)^2 \tag{11}$$

1.4. Boundary condition and initial condition

Flume inlet: Velocity inlet:

Inlet velocity is obtained by giving x , y and z velocity components ,in calm water flume inlet:

$$ui = 0 \tag{12}$$

in wave flume inlet:

$$\begin{aligned}
ux &= \tfrac{\pi H}{T}\tfrac{\cosh\kappa(y+d)}{\sinh\kappa d}\cos(\kappa x - \omega t) + \tfrac{3}{4}\tfrac{\pi H}{T}\left(\tfrac{\pi H}{L}\right)\tfrac{\cosh 2\kappa(y+d)}{\sinh^4\kappa d}\cos 2(\kappa x - \omega t)\\
uy &= \tfrac{\pi H}{T}\tfrac{\sinh\kappa(y+d)}{\sinh\kappa d}\sin(\kappa x - \omega t) + \tfrac{3}{4}\tfrac{\pi H}{T}\left(\tfrac{\pi H}{L}\right)\tfrac{\sinh 2\kappa(y+d)}{\sinh^4\kappa d}\sin 2(\kappa x - \omega t)\\
uz &= 0\\
\kappa &= \tfrac{2\pi}{\lambda}
\end{aligned} \tag{13}$$

Where H is wave height, T is wave period, λ is wavelength, h is water depth in flume.

Flume Outlet: Pressure outlet;

Flume sidewall: To reduce the influence of the sidewall, set it as a symmetry boundary;

Initial free surface: Set the water depth in the trough to 0.4m at the initial time.

Bottom of flume and side wall of pile: No-slip boundary condition;

$\boldsymbol{k - \omega}$: Given at the inlet and outlet, its value is estimated by the following formulas:

$$\begin{aligned}
k &= \tfrac{3}{2}(IU)^2\\
\omega &= \tfrac{\sqrt{k}}{\Omega_t}
\end{aligned} \tag{14}$$

1.5. Numerical wave flume

In order to explore the characteristics of the flow pattern around the monopile under the combined action of wave and vibration, a wave-vibrating cylindrical pile numerical simulation flume was constructed. For the convenience of the following description, a three-dimensional rectangular coordinate system is established with the positive direction of wave propagation in the flume as the X-axis, the height of the flume (from bottom to top) as the Y-axis, the width of the flume (from left to right facing the wave propagation direction) as the Z-axis, and the center point of the calm water horizontal plane at the entrance of the flume as the coordinate origin.

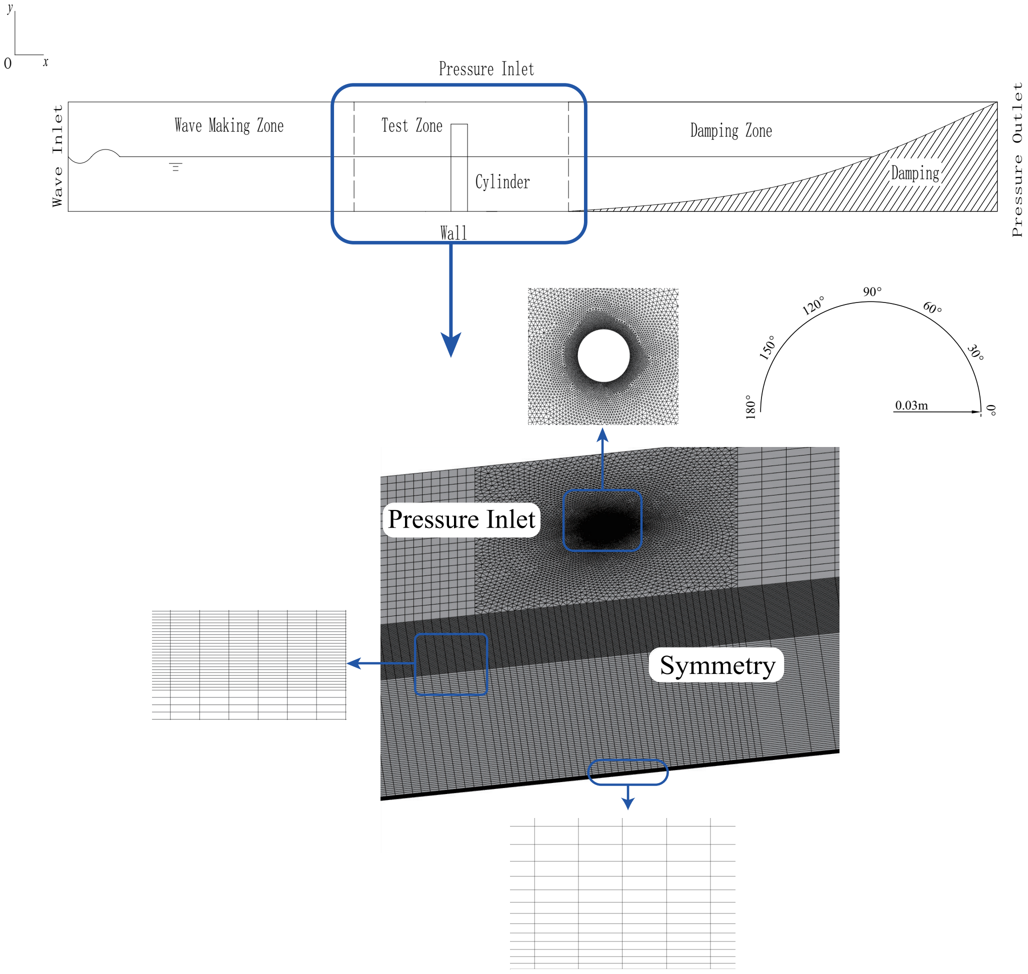

Figure 2. Sketch of the numerical wave flume and meshes

Along the positive direction of the x-axis, the flume is divided into three parts: the wave band, the test section and the end wave band. A cylindrical pile with a bottom radius of 0.06m and a height of 0.5m is arranged at the geometric center of the bottom of the test section. The width of the flume is 0.6m, the height is 0.5m, the water depth in the flume is 0.4m, and the lengths of the wave band, the test section and the end wave band are 4m, 1.5m and 11.2m respectively.

2. Working cases

2.1. Working cases in flume

This study involves 12 working conditions(Table 1), which can be classified into 3 groups: Cases1∼3 reproduce the classic experiments of Jesen and Koumoutsakos in flume to verify the turbulence model used; Cases4∼7 explored the development process of the flow field around the vibrating pile pile in the calm water flume; Cases8∼12 explored the change of flow regime under the wave-non vibration and wave-vibration in a wave flume. According to the boundary conditions, calm water surface would be generated in the calm water flume, while a second-order Stokes wave propagating along the X-axis direction would be generated in the wave flume. Dimensionless numbers KC_1 and KC_2 are defined to determine oscillation conditions of virbration pipe and wave:

$$
\begin{aligned}
KC_1 &= \frac{V_{\max} T_p}{D} \\
KC_2 &= \frac{U_{\max} T}{D}
\end{aligned}
\tag{15}
$$

where V_max is the maximum vibration velocity of pile, U_max is the maximum horizontal velocity of surface water quality point under wave condition, T_p is the the period of virbration pipe, T is the wave period, D is the characteristic length. In this study, D is the diameter of the monopile.

Table 1. Validation and numerical work cases

Index	$H(m)$	$T(s)$	$\lambda(m)$	$h(m)$	Re	KC_1	KC_2	KC_1/KC_2
Case1	-	9.7200	2.0000	0.2800	612920	76.3712	-	-
Case2	-	-	-	-	550	-	10.0000	-
Case3	-	-	-	-	9500	-	10.0000	-
Case4	-	-	-	0.4000	1764	-	0.5207	-
Case5	-	-	-	0.4000	3528	-	1.0413	-
Case6	-	-	-	0.4000	5292	-	1.5620	-
Case7	-	-	-	0.4000	7057	-	2.0827	-
Case8	0.0800	1.0572	1.6000	0.4000	14197	4.1902	0	0
Case9	0.0800	1.0572	1.6000	0.4000	14197	4.1902	0.5207	0.1243
Case10	0.0800	1.0572	1.6000	0.4000	14197	4.1902	1.0413	0.2485
Case11	0.0800	1.0572	1.6000	0.4000	14197	4.1902	1.5620	0.3728
Case12	0.0800	1.0572	1.6000	0.4000	14197	4.1902	2.0827	0.4970

Where Re is Reynolds number.

2.2. Monopile vibration

It is considered that the pile is a rigid body, there is a hinge at the bottom of the pile, and the pile vibrates in the same period with the wave from a certain time. Obviously, the displacement curve of the pile should conform to the characteristics of the periodic function. Figure 5 shows that the waveform is not stable at the beginning of calculation. In order to eliminate this effect, it is considered to start the pile after the waveform is stable. Based on the above considerations, the motion mode of the pile is set as: at the initial stage, the pile is fixed at the bottom of the flume, and then a small disturbance is given to it at a predetermined time to obtain the initial velocity v_0. Then the velocity of the pile changes according to the cosine function curve, which makes the pile vibrate periodically. In order to avoid the function singularity caused by the sudden change of flow velocity, a short function transition is adopted in the pile start-up stage (near t_0):

$$
ux = \begin{cases} 0, 0 < t < (t - \delta t) \\ \frac{V_m}{2}[\cos(c(t - t_0)) + 1], (t_0 - \delta t) < t < t_0 \\ V_m \cos(\sigma(t - t_0)), \quad t > t_0 \end{cases}
\tag{16}
$$

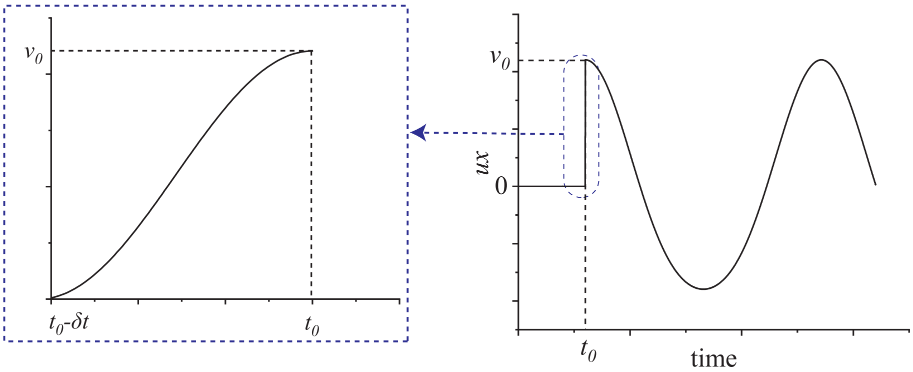

Figure 3. Movement track of monopile along X-axis.

δt determined by the time step, the value in this study is 0.0050s; t_0 represents the initial time of the pile, σ is frequency, $\sigma = \frac{2\pi}{T}$, c is the constant used to control the period of the transition function, $c = \frac{\pi}{\delta t}$. The initial moment of pile vibration is the same as that of wave equilibrium. Based on the above considerations, the pile in Cases 8∼11 start to vibrate in 6.0210s.

2.3. Dynamic meshes

The research method of Leeref-5 is that the pile is fixed, and the impulse start or stop of the pile is equivalent by the change of inlet-velocity. However, due to the existence of wave making inlet the change of inlet-velocity is bound to affect the generation of wave, so a similar scheme cannot be adopted in this study.

Therefore, in order to simulate the vibration of monopile, it is necessary to use the dynamic mesh method in the pile wall. In order to ensure the quality of the cells after remeshing, all the cells in the domain area are marked, and the cells are stretched or reconstructed in each time step.

Under the above settings, the remeshing is "absorbed" by all the cells in the domain, so the deformation of a single cell has minor change, and the cells quality degradation and calculation result error caused by a large number of grid reconstruction are avoided.

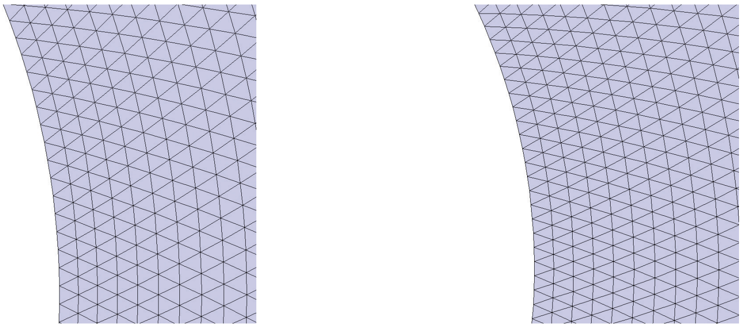

Figure 4. Maximum displacement cell(case7, $\omega t = 9°$) has minor deformation compared with the initial cell. Through the check of the minimum cell, it can be concluded that the side length of the minimum cell at this time is 81.6657% of the original, and it is basically stretched and tilted. It can be seen that a single grid has minor change.

3. Validation of numerical model

3.1. Validation of VOF model

3.1.1. Results of wave making and absorbing

Table 2 shows the wave parameters used in this study:

Table 2. Stokes II wave parameters

Wave	h/m	H/m	λ/m	T/s
StokesII	0.4000	0.0800	1.6000	1.0572

According to the Second order Stokes wave theory, the wave surface equation of this waveform can be obtained:

$$\begin{aligned}
&\eta = -\frac{\kappa A^2}{2\sinh 2\kappa h} + A\cos(\kappa x - \sigma t) + \frac{A^2\kappa}{4}\frac{\cosh\kappa h\cdot(\cosh 2\kappa h + 2)}{\sinh^3(\kappa h)}\cos(2\kappa x - 2\sigma t)\\
&A_2 = \frac{H}{2}\\
&\kappa = \frac{2\pi}{\lambda}\\
&\sigma = \frac{2\pi}{T}
\end{aligned} \tag{17}$$

Figure 5 shows the comparison between the theoretical wave surface and the numerical results:

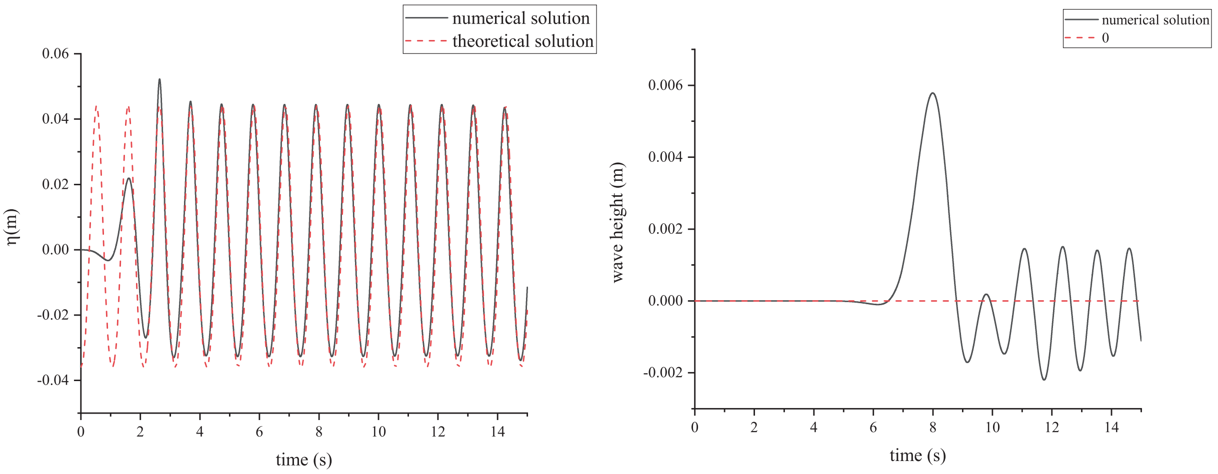

Figure 5. Stokes wave: theoretical waveform, calculated waveform and wave absorb

To compare the wave making effect, calculate the phase average value of the numerical solution:

$$u = \frac{1}{N}\sum_{n=0}^{N} u(t + nT) \tag{18}$$

u is the phase average value of wave parameters, where the peak height, trough height and period are taken. Table 3 shows the phase average waveform parameters obtained by numerical calculation:

Table 3. Phase average value of wave parameters

Index	$wavecrest/m$	$wavetrough/m$	$pried/s$
Numerical solution	0.0445	-0.0336	1.0595
Theoretical solution	0.0442	-0.0359	1.0572

The error between the numerical solution and the theoretical solution is very small, which reflects the well wave making result.

Figure 5 also shows the wave surface at one wavelength from the outlet. The wave height is attenuated to less than 5% of the original wave height, and the wave absorb has achieved well result.

3.1.2. Influence of monopile and symmetry wall on wave propagation

In order to verify the influence of piles on wave propagation, the wave height time history at $x = 0$, 0.075m from the center of the pile and 0.05m from the side wall were measured. For comparison, a flume without piles is set up, and the waveform of the center of the flume with $x = 0$ is measured. Figure 6 that the wave height time history of the three are almost the same, and the influence of the pile and the side wall on the wave propagation is negligible.

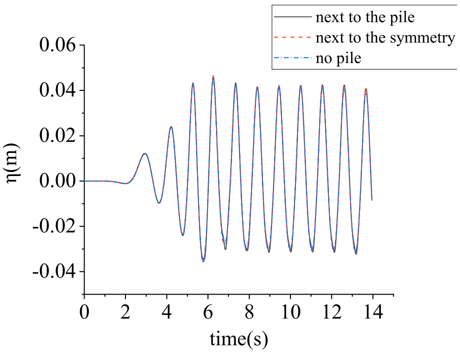

Figure 6. The wave surfaces next to the pipe, the symmetry and in the no pile flume.

3.1.3. Wave height attenuation along the flume

Due to the existence of dissipation term, the wave height may decay along the flume. Figure 7 shows the phase average change of wave height along the flume. The monitoring results show that the phase average wave height of Stokes wave decays from 0.07892m to 0.07074m. Table 4 shows the attenuation waveform parameters:

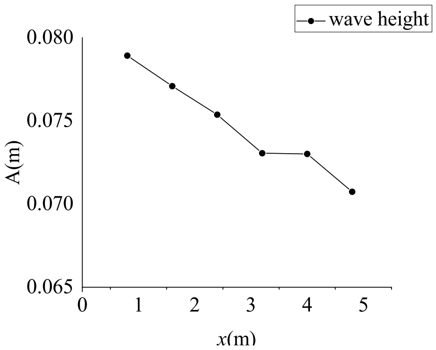

Figure 7. Attenuation of wave height

Table 4. Attenuation wave parameter

Index	*Wave steepness*	*Relative height*	*Ursell number*
Attenuation wave	0.0442	0.1768	2.8296
Theoretical range(StokesII)	(0,0.055)	(0,0.5)	(0,25)

The second-order Stokes wave theory is still applicable to the attenuated wave and not affect the conclusion of this study.

3.2. Validation of turbulence model

3.2.1. Analysis of meshes sensitivity

Before the calculation, three sets of different meshes are used to test the meshes sensitivity. The height of the first layer of three sets of meshes near the bottom surface is

0.1mm, 0.2mm and 0.5mm respectively (Table 5) . In this study, the velocity distribution near the bottom surface is a hydraulic factor that needs special attention.

Figure 8 shows the velocity distribution near the bottom surface in the X-direction. As comparison mainstream velocity distribution results shown, the difference among three sets of different meshes is very minute. However, in the area near the bottom surface, the calculated results of mesh3 are quite different from those of Mesh1 and Mesh2. By Mesh3, it is difficult to accurately capture the velocity distribution characteristics in the boundary layer. In comparison, the difference between the calculation results of Mesh1 and Mesh2 is very minute, which indicates that setting the height of the first layer of meshes to 0.2mm is enough to capture the velocity characteristics. It should be considered that too minute the height of the first layer of meshes lead to too large the ratio of mesh length to height and poor meshes quality, and a sharp increase in the number of meshes in the boundary layer, which affect the computational efficiency. Based on the above reasons, Mesh2 is selected as the near bottom mesh generation scheme.

Table 5. Mesh schemes of velocity distribution tests.

Index	y/mm	$Growth\ rate$	$Number\ of\ layer\ grids$
Mesh1	0.15	1.05	30
Mesh2	0.25	1.05	20
Mesh3	0.60	1.05	10

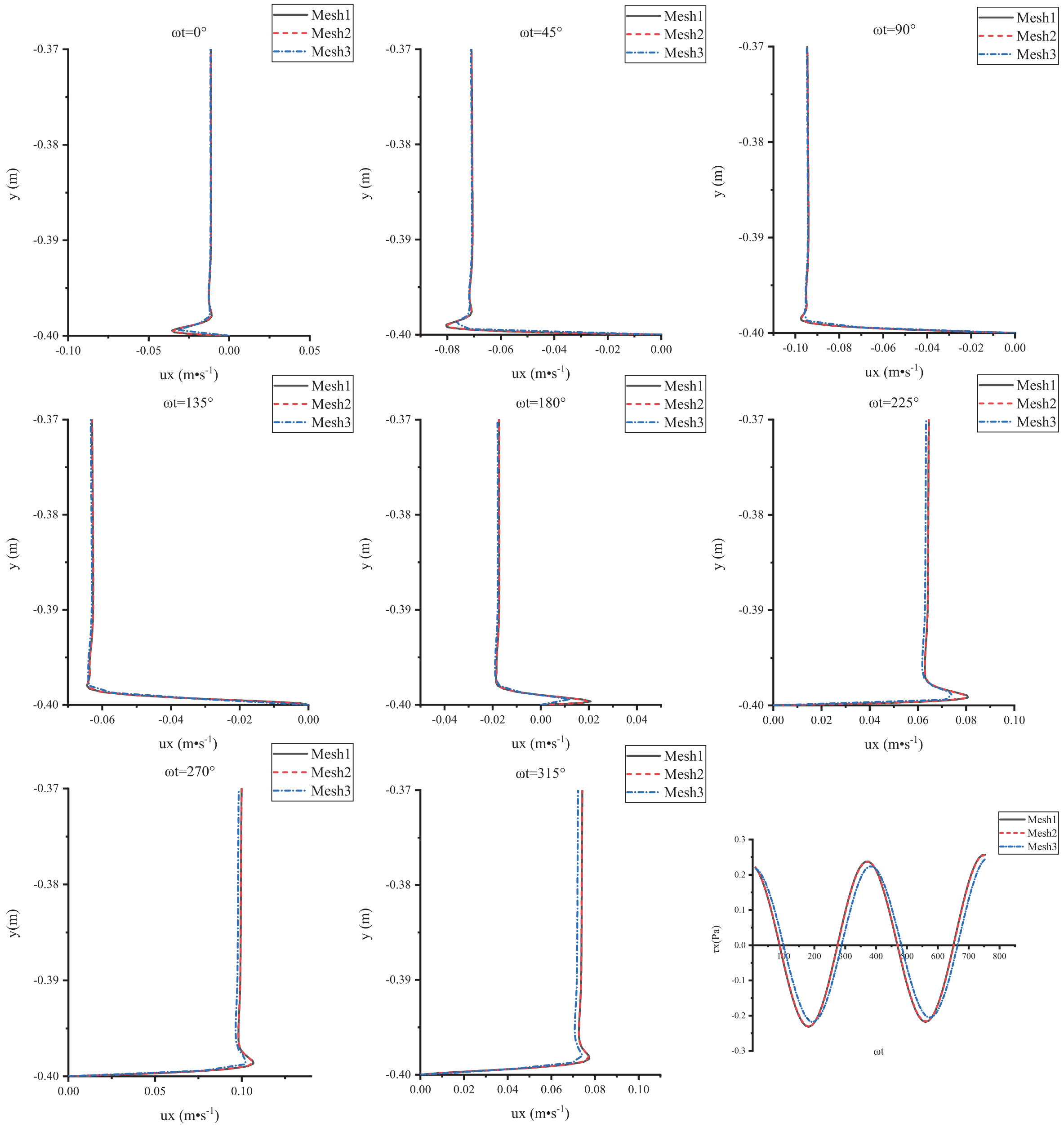

Figure 8. Near bed velocity distribution and bed shear stress time history of mesh1, Mesh2 and mesh3.

The variation of the pressure coefficient and vorticity distribution of the pile side wall is directly related to the development and shedding of vortices. Therefore, it is necessary to test the sensitivity of the near wall meshes of the pile side wall. The test objects are Mesh4, Mesh5 and Mesh6 (Table 6) .

The error between the pressure coefficient results of the three sets of meshes is minute, but the calculation results of Mesh6 are smaller than Mesh4 and Mesh5 near the inflection point of the pressure coefficient. The vorticity is significantly affected by the grid than the pressure coefficient. Figure 9 shows that mesh6 scheme is not able to correctly capture the vorticity distribution characteristics, while mesh4 and mesh5 have this ability. After comprehensive consideration, Mesh5 is selected as the near pile side mesh generation scheme.

Table 6. Mesh schemes of pressure coefficient and vorticity distribution tests.

Index	*y/mm*	*Growthrate*	*Numberoflayergrids*
Mesh1	0.20	1.05	30
Mesh2	0.30	1.05	20
Mesh3	0.60	1.05	10

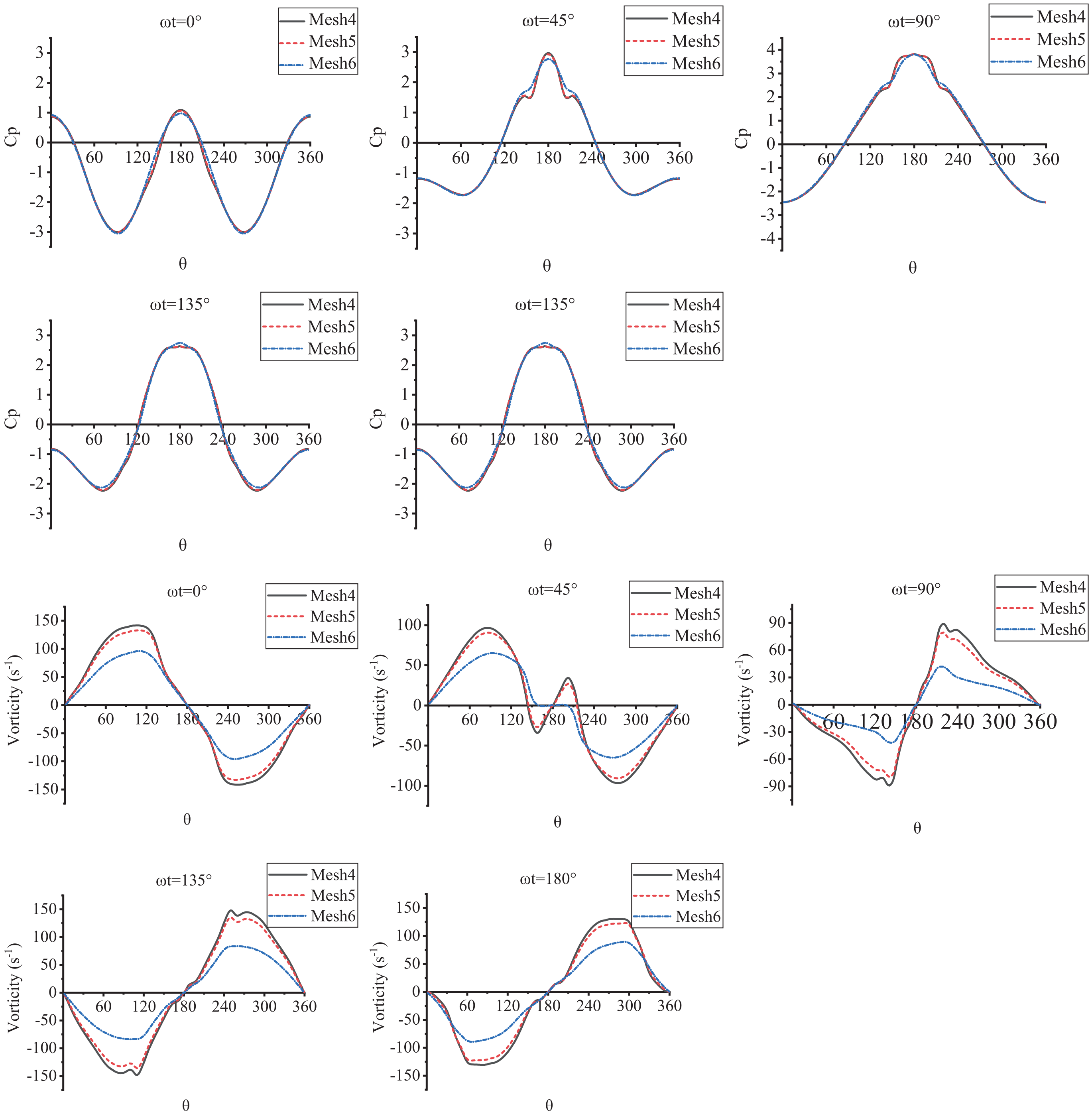

Figure 9. Distribution of monopile side wall pressure coefficient(Cp) and vorticity of mesh4, mesh5 and mesh6 (y=-0.3m) .

3.2.2. Analysis of Yplus value

The precision meshes is designed for the calculation of unsteady flow under the combined influence of cylindrical vibration and wave action, so the height of the first layer of meshes near the wall is very important. This height is represented by the Yplus value. The Yplus value is defined as:

$$y^{+} = \frac{y\rho u_{\tau}}{\mu} \tag{19}$$

This value indicates the ability of the near wall meshes to capture the flow field characteristics. The SST model requires the Yplus value to be within (0,10) to ensure that the $k - \omega$ equation is used near the wall and that the centers of the first layer of meshes falls in the viscous sublayer. The mesh generation scheme of Mesh2+Mesh5 is selected, and the Figure 10 shows that Yplus value is basically about 1, which meets the mesh requirements of the numerical model.

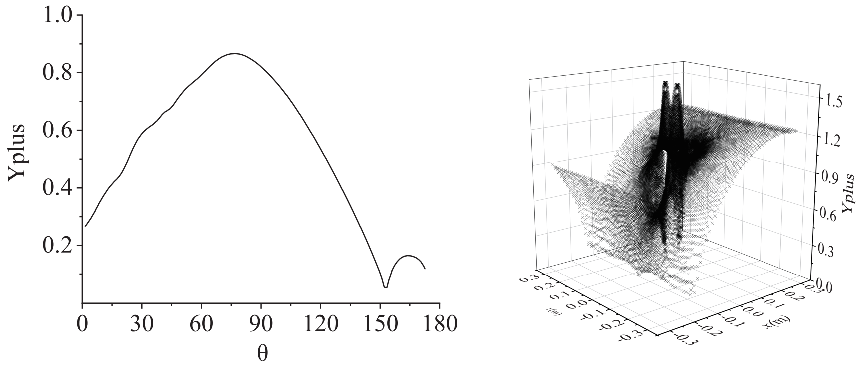

Figure 10. Yplus value distribution of monopile side wall and bed surface shows that its value is about 1.

3.2.3. Comparison with classical studies of oscillating flow and flow around impulsively piles

Jensen's test[26] showed the influence of oscillating flow on the velocity distribution near the bottom surface. Figure 11 shows that the velocity distribution near the bottom of the test pipe was measured using an air pump oscillating flow test device.

doi:10.20944/preprints202208.0270.v1

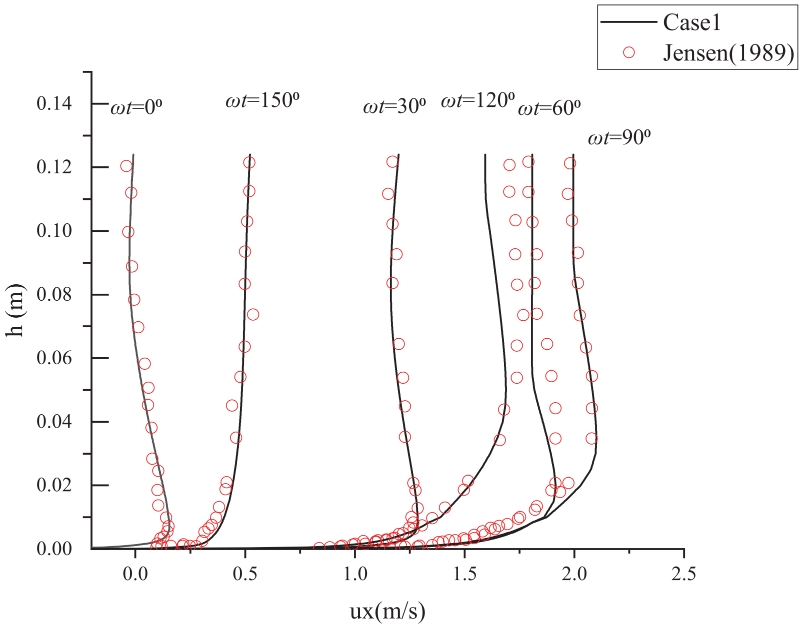

Figure 11. Comparison of velocity distribution near the bottom in case1 and Jensen's test. Jensen introduced dimensionless velocity.

The flow pattern around piles is another important factor in this study. Koumoutsakos summarized the change law of unsteady flow field around impulsively piles[6], which has been recognized by many researchers(Figure 12).

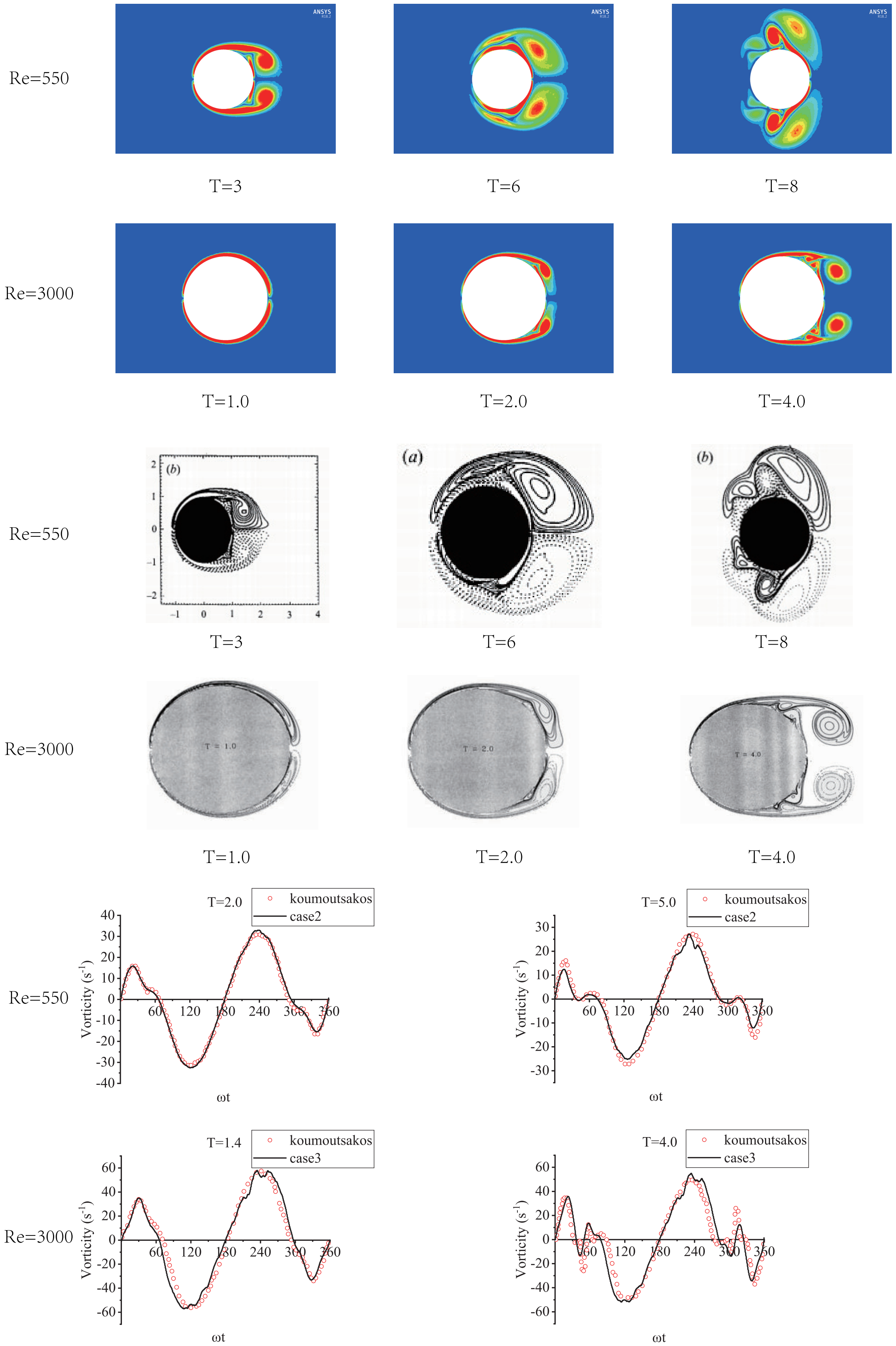

Figure 12. The vortex fields and surface vorticity in the case of re=550 and re=3000 obtained from the study of case2, case3 and Koumoutsakos.

doi:10.20944/preprints202208.0270.v1

The above results show that the numerical model used in this study is effective in oscillating flow simulation and pile vibration simulation.

4. Results and discussion

This section provides the calculation results of vortex fields, monopile surface vorticity, shear stress distribution, shear stress time history and phase lead in calm water flume and wave flume. At the same time, the causes for the change of vortex fields and shear stress are discussed, and the influence of KC_1 on vortex fields and shear stress is also compared and discussed. In case4∼7, the time of $\omega t = 0^\circ$ is 0.210s, and in case8∼12, the time of $\omega t = 0^\circ$ is 7.078s.

4.1. Vortex identification

The vortex is commonly caused by the combined action of the shear around the pile, and the adverse pressure gradient produced due to the presence of the pile. The Ω-criterion decomposes vorticity ω_L into a rotating part and a non-rotating part:

$$\omega_L = R + S \tag{20}$$

where R represents the vorticity of the rotating part and S denotes the vorticity of the non-rotating part. Subsequently, a numerical value Ω_L is introduced to represent the proportion of the rotating vorticity to the total vorticity, that is, a threshold insensitive vortex identification method is evaluated[27,28]:

$$\Omega_L = \frac{\|B\|_F^2}{\|A\|_F^2 + \|B\|_F^2 + \varepsilon} \tag{21}$$

Evidently, the value range of Ω is (0,1). In the case of Ω higher than 0.5 (generally 0.52), B is the dominant factor (i.e., the rotating part), which can be considered as vortex formation.

4.2. In calm water flume

4.2.1. Vortex fields around monopile in low KC_1

Figure 13 presents the vortices shedding at the front and rear of the vibrating pile in calm water. As the pile swings back and forth, shedding vortices periodically appear in the front and behind of the pile. Because the velocity difference in depth is far less than that under the wave condition, the vortices surfaces do not stretch obliquely with the water depth direction. With the increase of KC_1, the vortices field exhibits various characteristics. By this view, the following two cases can be considered and discussed:

From the distribution of the pressure coefficient along the circumference(Figure 9), it can be seen that at the equilibrium position of the pile vibration, the reverse pressure gradient region appears behind the side of the pile motion direction, which is similar to the general flow around the pile. The difference is that with the vibration of the pile, the direction of the flow around the pile changes periodically, and the position of the inverse pressure gradient region also changes periodically, and there are acceleration and deceleration stages. Under the influence of periodic motion, the primary vortices have reattachment and periodic reappearance. For example, the vortex fields can observe the phenomenon of vortices reattachment at $\theta = 150^\circ$. Due to the periodic vibration of the pile, the velocity around the pile exhibits the characteristics of periodic acceleration and deceleration, which makes the shedding vortices lack sufficient power to diffuse forward and backward to the pile. The periodic direction changes of flow velocity and the reattachment of the vortices hinders the diffusion of the shedding primary vortices to the downstream.

In Case5 and Case6, the secondary vortices become obvious, and the vortices shedding angle is $\theta = 160^\circ$. However, their evolutions are limited by the primary vortices and reattchment effect. The secondary vortices tend to penetrate the primary vortices, but it cannot reach the external irrotational flow field. The primary vortices shed from the side wall, and their vortex strengths reduce through diffusion, preventing the growth of the secondary vortices. After that, the displacement direction of the pile alters such that the secondary vortices reattach to the wall again.

As the further increase of KC_1, the vortex intensity of the primary vortices and the secondary vortices increase, but the primary vortices and the secondary vortices are still limited by the reattachment effect. It is worth noting that the secondary vortices are more obvious, and has a more obvious shedding trend than case4 and 5 at the time of $\omega t = 180^\circ$. However, the influence of reattachment cannot be avoided. During the movement of the pile in the negative direction of the X-axis, it can be observed that the primary vortices and the secondary vortices reattach at the position of $\theta = 160^\circ$and overlapped each other.

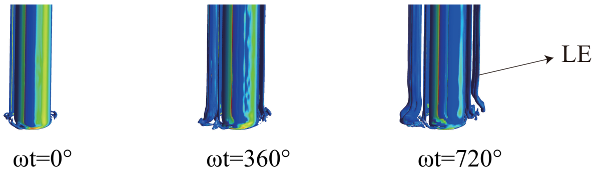

Figure 13. Lee wake vortices around the pile of case7. The Lee wake vortices of case4~6 is not easy to shed, and the phenomenon is not obvious. Therefore, in the following, the vortex fields section is taken at the position of y=-0.3m.

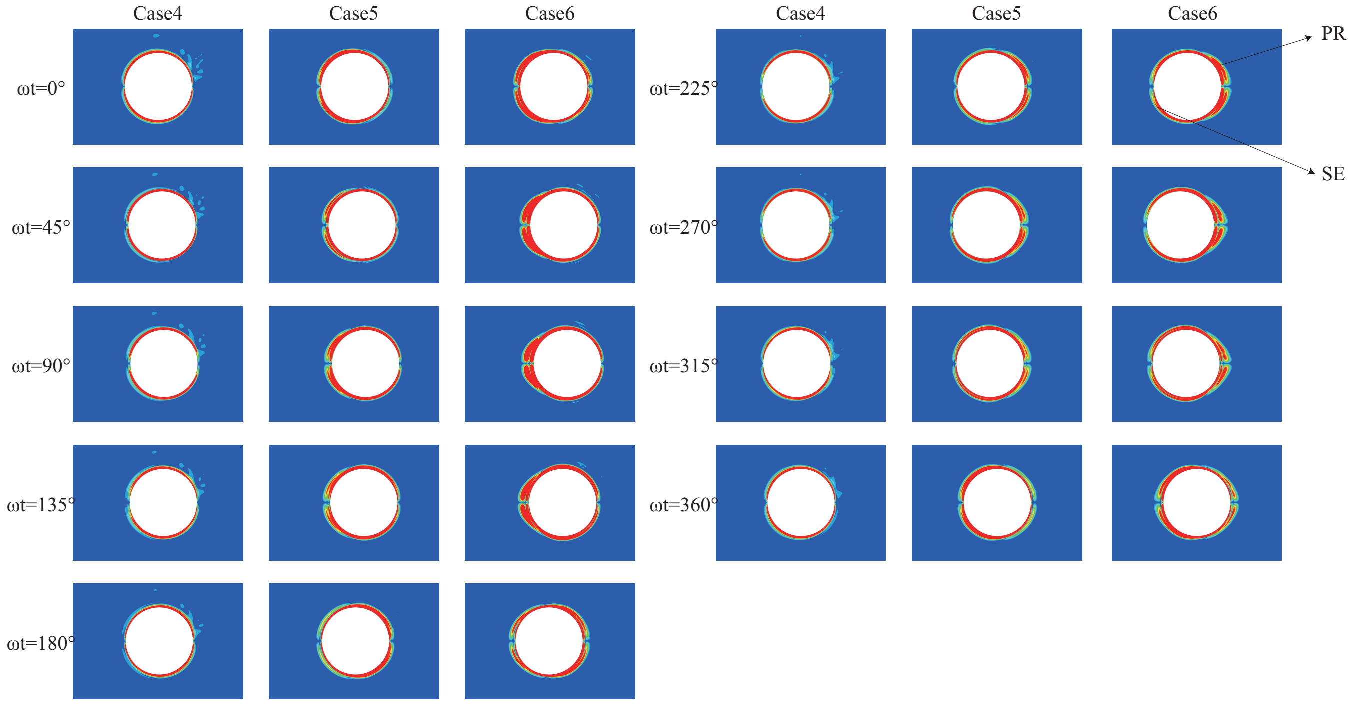

Figure 14. The distribution of vortex fields around the pile in case4~6, Pr is the primary vortices, and Se is the secondary vortices. (more obvious in case5)

4.2.2. Changes in vortex field in high KC_1

With the growth of amplitude in the same period, the vortex fields around the pile changes again. The strengths of the primary vortices are high. At the same time, as the amplitude becomes larger, there is enough space for the development of the shedding vortices, and the influence of the reattachment phenomenon is further weakened. Therefore, the biggest difference between the distribution of the vortex fields in case7 and cases4~6 is that the vortices are completely shed, and the vortex field in case7 loses the characteristics of periodic recurrence.

Figure 15 illustrates that the primary vortices shed from $\theta = 165^\circ$ and diffuses to the "temporary" wake area under the action of inertia and negative flow. After that, the displacement direction of the pile varies, the flow becomes positive flow, and the primary vortices are forced to reattach. However, the energy of the vortices does not dissipate, and the displacement direction of the pile turns to the positive and backward directions of the X-axis again. The primary vortices quickly shed, is pulled and torn by the negative flow, and small vortex shed.

Similarly, on the other side of the pile, the primary vortices are separated, elongated and split. After that, the secondary vortices shed from the sidewall again, and the above process is repeated. It is worth mentioning that the shedding small vortices are "caught up" and swallowed up by the primary vortices forced to move with the pile, which once again reflects that the deceleration process of vibration and the periodic direction changes of flow velocity hinder the propagations of the vortices to the "downstream".

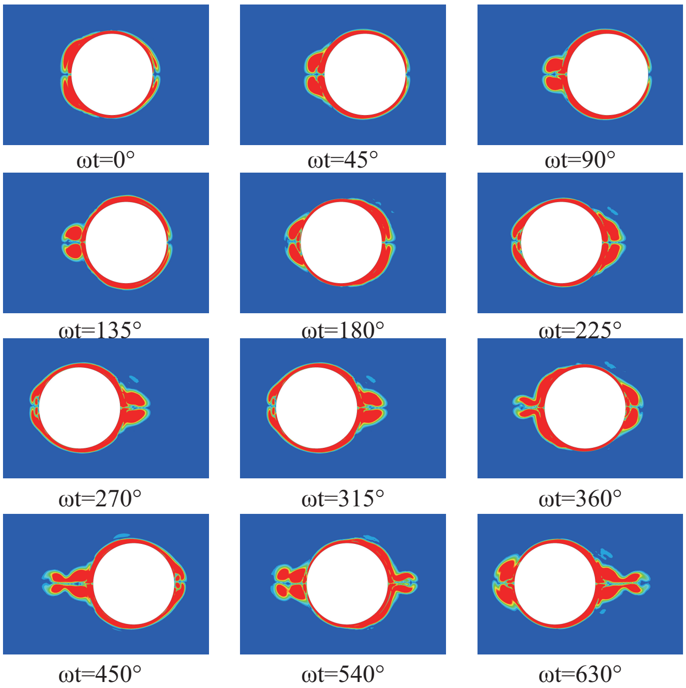

ωt=0° ωt=45° ωt=90°

ωt=135° ωt=180° ωt=225°

ωt=270° ωt=315° ωt=360°

ωt=450° ωt=540° ωt=630°

Figure 15. Vortex field distribution around the pile of case7. Shedding vortices are easily observed.

4.2.3. Variation of vorticity on monopile surface

The vorticity on the surface of the pile can more clearly show the development of the vortex fields on the side wall of the pile in Figure 16. At the time of high velocity of $\omega t = 0^\circ$, 180°, and 360°, the vorticity on the pile surface increases linearly with the increase of KC_1. It is easy to comprehend that the velocity around the pile increases linearly with the increase of KC_1. At the same time, with the continuous change of the vibration direction of the pile, the positive and negative values of vorticity also alternately vary.

In cases4$\sim$7, the vortex fields present symmetry, which is also reflected in the figure. A notable change is that at the time after $\omega t = 360^\circ$, the peak value of surface vorticity of case7 shifted, and at the time of $\omega t = 540^\circ$, it moved to $\theta = 0^\circ$ offset, and at $\omega t = 720^\circ$, it is $\theta = 180^\circ$ offset, that is, with the increase of the surface velocity of the pile sidewall, the peak value of the surface vorticity shifts to the wake region.

At $\omega t = 90^\circ$and 270°, the flow velocity is low, and the vorticity no longer increases linearly with the increase of KC_1. The peak value of surface vorticity of case7 is 2 orders of magnitude higher than that of case4. It is worth noting that at $\omega t = 270^\circ$, there is an obvious secondary peak at $\theta = 150^\circ$, which shows that with the increase of KC_1, the influence of the reattachment vortices on surface vorticity becomes more and more obvious.

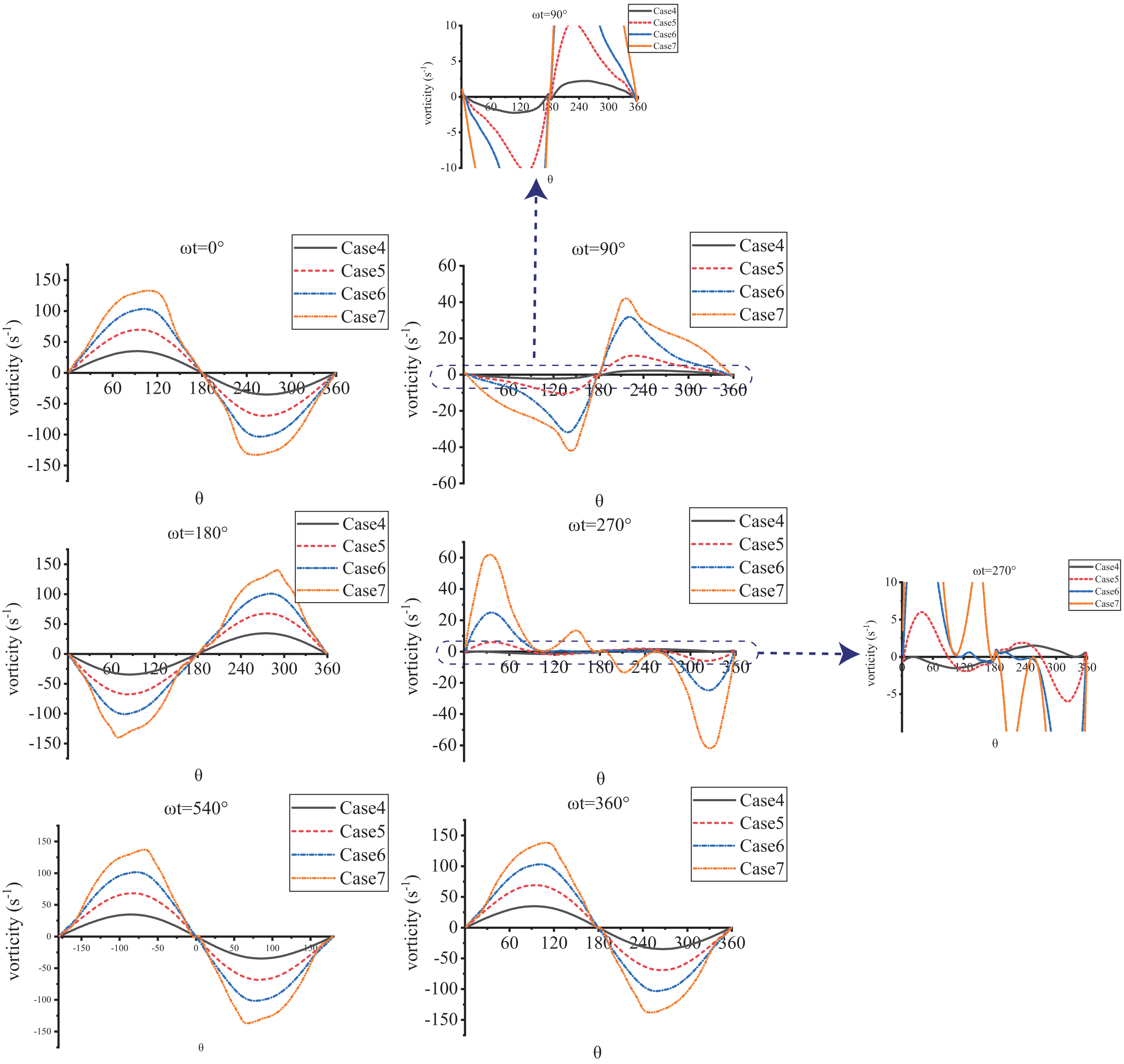

Figure 16. Vorticity distribution on the monopile surface.

4.2.4. Overall distribution of bed shear stress 382

A crucial effect of the periodical variation of the flow velocity in the main flow area is that it affects the distribution of the bed shear stress. Figure 17 demonstrates the overall variation of the bed shear stress around the pile with the vibration of the pile in cases4 $\sim$ 7. At the front of the pile, the vibration of the pile causes inverse flow. With the vibration of the pile, the inverse flow region alternately appears in front of and behind the pile. Due to the constant change of the inverse flow velocity and weak inverse flow intensity, it is difficult to configure a complete horseshoe vortex structure. Only an unformed horseshoe vortex structure is configured in front of and behind the pile of case7, which affects the bed shear stress in this area, making that present an irregular saddle shape. 383 384 385 386 387 388 389 390 391

Regarding the shear flow region on the side of the pile, by capturing the maximum point of the bed shear stress, it can be noted that the maximum shear stress on the side of the pile alternates between $\theta = 85^\circ$ and $\theta = 95^\circ$ on the side of the pile (case 4). The distribution of shear stress in case5$\sim$case7 is very similar to that in case4, but the alternating 392 393 394 395 range of the maximum shear stress is different. Cases5∼7 reach $(78^\circ, 102^\circ)$, $(72^\circ, 108^\circ)$, and $(62^\circ, 118^\circ)$, respectively. In general, as the increase of KC_1, the vibration intensity increase, and then the area under the influence of the vibration enlarges.

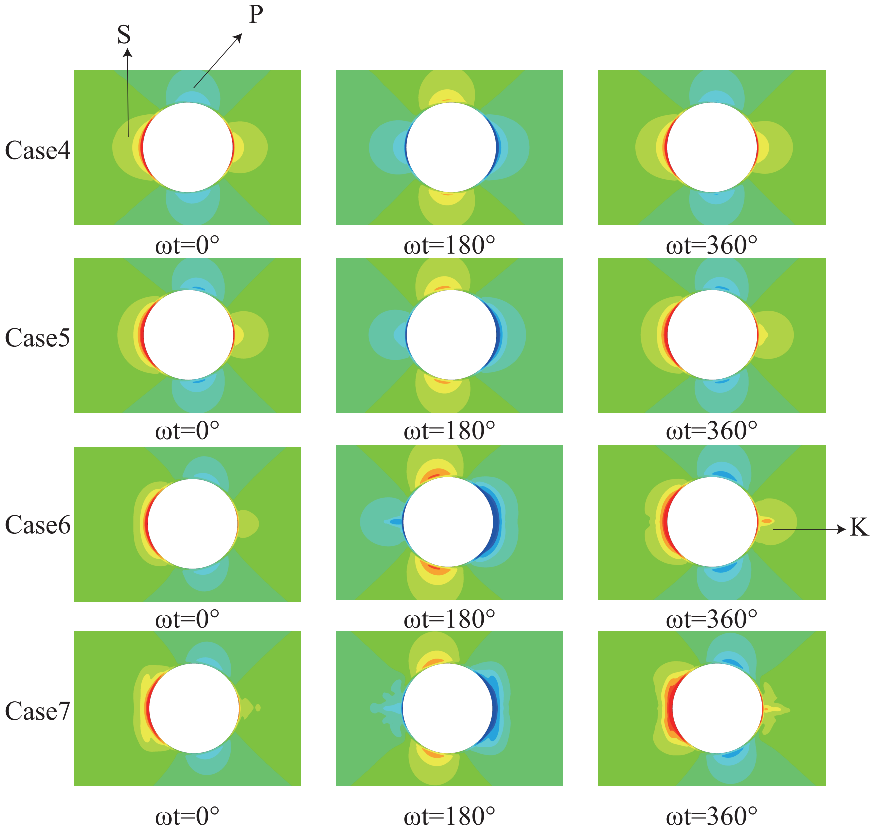

Figure 17. The overall distribution of shear stress around the pile of case3 to case6. S is the high stress area caused by inverse flow, P is the high stress area caused by shear flow, and K is the high stress area elongated after the movement direction of the pile is changed.

4.2.5. Phase Lead

Figure 18 and Figure 19 shows the time history of flow velocity and bed shear stress at the measuring points. The coordinate of bed shear stress measuring points is (0,-0.4,0.04). d is the vertical distance from flow velocity measuring points to bed shear stress measuring points. $\delta\phi_1$ is onshore angle, $\delta\phi_2$ is offshore angle. The "phase lead" effect originates from the upper edge of the boundary layer, and the closer it is to the bed surface, the more obvious it is. On the side of the pile, the shear stress changes periodically, but there is a phase difference with the velocity of free stream. This is consistent with the conclusion of the classical oscillating flow test. Compared with the research results of van der, due to the low shear velocity in this study, the phase lead angle in case3 is larger, reaching 42.06°in the onshore flow and 40.86°in the offshore flow, which is close to the analytical solution(45°) of the phase lead effect in the laminar flow.

It is worth noting that with the increase of KC_1, the time history curve of bed shear stress shows a peak shape. In this case, the phase lead effect still exists, but it is difficult to measure at the equilibrium position. This phenomenon is related to the influence of pile vibration on the lateral shear acceleration zone of the pile. In fact, the reciprocating motion of the pile not only causes the appearance of the shear zone on the side of the pile, but also causes the driving flow between the shear zone and the wake zone, resulting in the deviation of the time history curve of the bed shear stress. Based on this, this study uses the peak phase and valley phase of flow velocity period and shear stress period to measure the phase lead angle. With the increase of the relative velocity of pile vibration, the phase leading angle decreases significantly, which is consistent with the research results of van der.

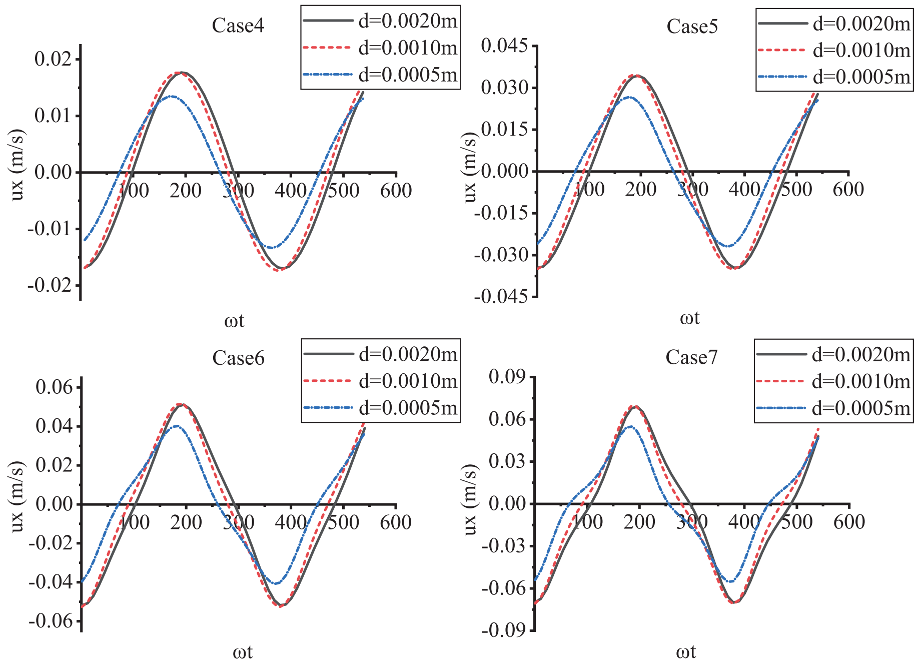

Figure 18. Phase lead effect in calm water flume(boundary layer).

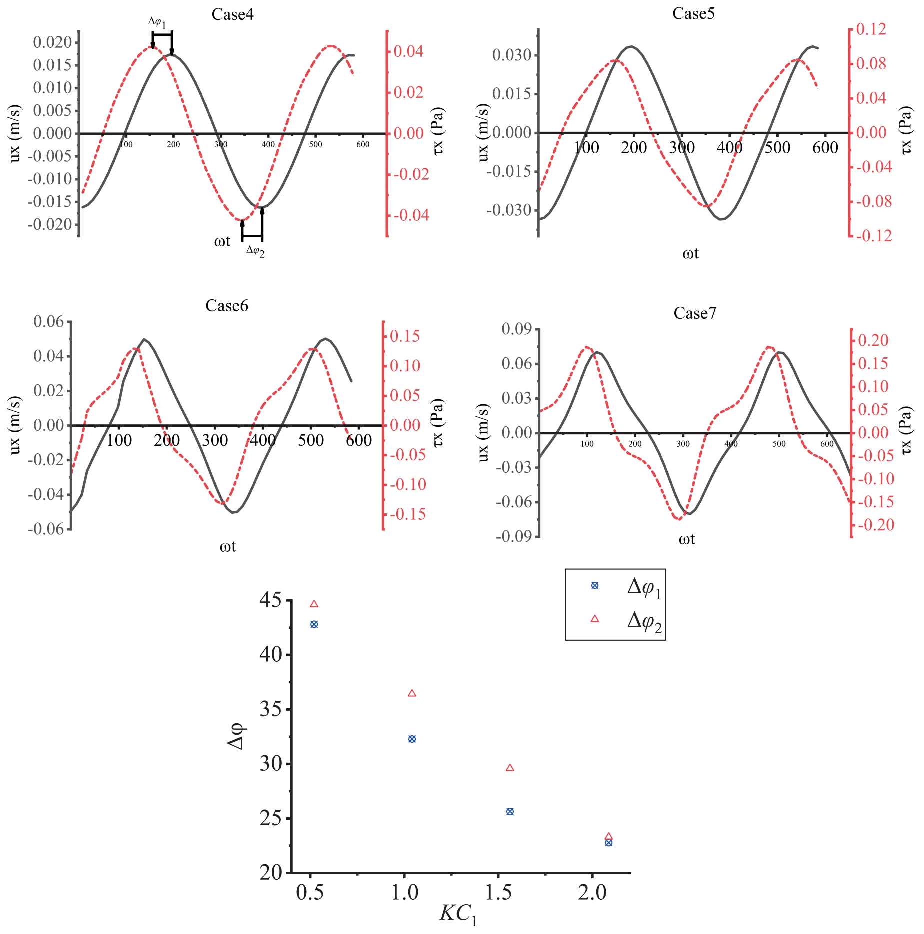

Figure 19. Phase lead effect in calm water flume (bed shear stress) and phase angle.

4.2.6. Influence of vortices around monopile

In the front and behind of the pile, the vibration of the pile causes the backflow near the bed surface, forming horseshoe vortices. With the vibration of the pile, horseshoe vortices appear alternately in front of and behind the pile, and correspondingly, high shear stress areas appear alternately in front and behind of the pile. After the movement direction of the pile changes, a temporary wake zone is formed. In the area near the bed surface of this region, the previously formed horseshoe vortices have not completely dissipated, and are stretched and broken (Figure 21). Under its influence, a slightly stretched high stress area appears on the bed surface. The difference between case4∼6 and case7 is that the Lee wake vortices that fall off smoothly forms a U-shaped vortex structure near the bed surface under tension, which affects the velocity distribution and bed shear stress at this position. Figure 20 shows that the time history curve of bed shear stress (the coordinate of bed shear stress measuring point is (-0.07,-0.4,0)) has a prominent peak, which occurs when the pile approaches the measuring point. In addition, the value of the shear stress in the time history of the pile approaching the measuring point is significantly higher than that of the pile away from the measuring point, which reflects the influence of vortices on the change of the bed shear stress in this area.

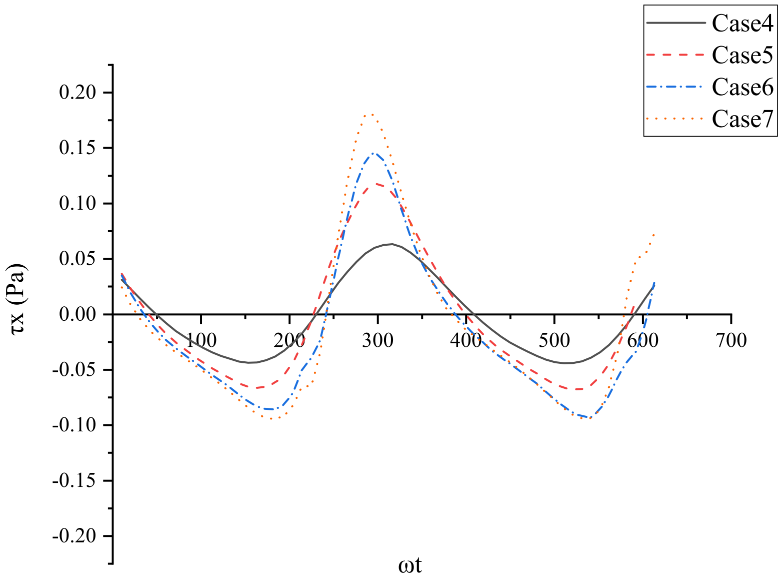

Figure 20. Time history of bed shear stress.

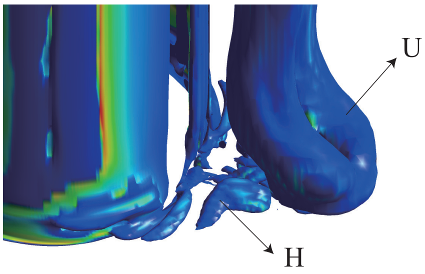

Figure 21. Horseshoe vortices structure H broken by tension and U-shaped vortex structure U formed by tension of Lee wake vortices in case7.

4.3. In wave flume

4.3.1. Vortex fields around the monopile

According to wave dynamics theory, the velocity of a water particle in wave flume is

$$\begin{aligned}
ux &= A\left[\frac{A\kappa}{2}\frac{\cosh 2\kappa(z_0+h)}{\sinh^2\kappa h}\omega + \frac{\cosh\kappa(z_0+h)}{\sinh\kappa h}\cos\theta_0 + \frac{A\kappa}{2\sinh^2\kappa h}\left[1-\frac{3}{2}\frac{\cosh 2\kappa(z_0+h)}{\sinh^2\kappa h}\right]\cos 2\theta_0\right]\\
uy &= A\left[-\frac{\sinh\kappa(z_0+h)}{\sinh\kappa h}\sin\theta_0 + \frac{3}{4}A\kappa\frac{\sinh 2\kappa(z_0+h)}{\sinh^4\kappa h}\sin 2\theta_0\right]\\
uz &= 0\\
\theta_0 &= \kappa x_0 - \omega t
\end{aligned} \tag{22}$$

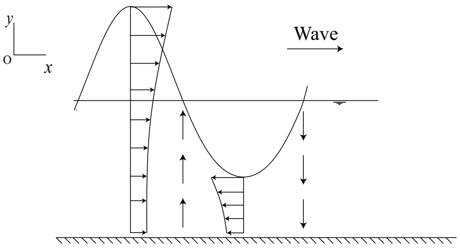

Figure 22. The velocity of wave water particle

It can be noted that the velocity in the X-axis direction is divided into two parts: a periodic term and aperiodic term, which indicates that there is horizontal displacement while the water quality point moves along the periodic trajectory. Moreover, along the direction of water depth, the velocity of water quality points increases from the bottom to the surface. Under the influence of lateral shear flow, Lee-wake vortices are generated around the pile. Figure 23 shows that the Lee-wake vortices behind the pile are more obvious than those in front of the pile and are affected by the wave propagation direction. This corresponds to Bakey's result[7].

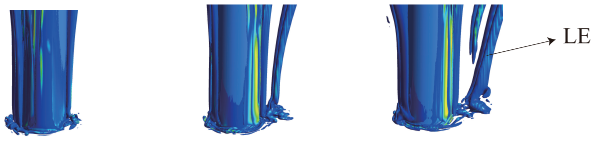

ωt=0° ωt=360° ωt=720°

Figure 23. The Lee wake vortices around the pile of case8 show that the Lee wake vortices behind the pile are significantly stronger than that in front of the pile

Figure 24 shows the time history development of the vortex fields. Different from the general flow around a pile, in this study, when the wave crest passes through the pile, the free stream mainly moves in the positive direction of the X-axis, and the Lee-wake vortices surfaces on the back of the pile are continuously elongated. In contrast, when the wave trough passes through the pile, the free stream mainly moves along the negative direction of the X-axis, and the Lee-wake vortices surfaces in front of the pile are continuously elongated. Due to the uneven distribution of wave velocity in the direction of water depth, the downstream diffusion velocity of these vortices' changes with the change in water depth. As shown in the figure, the flow velocity near the bed surface is low, and the flow velocity at the upper end of the pile column is high. Under the influence of this velocity difference, the tandem vortices are elongated and tilted and may be "broken". Under the wave-vibration combine influence, one wave period is divided into four stages:

$\omega t \in (0,90)$: At this stage, the wave water quality point movement flows from descending to horizontal flow in the positive direction of the X-axis, and the pile slows down along the positive direction of the X-axis. The vortex field of 90° shows that after the pile moves, the vortices in front of the pile are easier to shed due to inertia than under the condition of no vibration. Simultaneously, the vortices behind the pile reappear.

$\omega t \in (90, 180)$: At this stage, the wave water point movement changes from horizontal flow in the positive direction of the X-axis to upwelling, and the pile accelerates along the negative direction of the X-axis. When the wall-attached vortices behind the pile under the combined action of the X-axis forward flow formed by the pile movement, the vortices in front of the pile completely shed.

$\omega t \in (180, 270)$: At this stage, the wave water quality point movement flows from rising to horizontal flow in the negative direction of the X-axis, and the pile slows down along the negative direction of the X-axis. The vortices shed at 120° is reattached under the action of horizontal flow in the negative direction of the X-axis.

$\omega t \in (270, 360)$: At this stage, the movement of wave water quality points changes from horizontal flow in the negative direction of the X-axis to downwards flow, and the pile accelerates along the positive direction of the X-axis. The movement of the pile once again "helps" the shedding of the vortices in front of the pile. The vortices behind the pile that are previously shed is far from the pile under the action of wave propagation and drifting, and no reattachment has occurred.

In general, the pile vibration affects the development of the vortex fields in the form of disturbance, but this small disturbance can significantly interfere with the development process of the vortex field. The calculation results show that the strength of the reattachment vortices change during the increase in KC_1/KC_2, resulting in the obvious difference between the vortex fields of cases 8, 9 or 10 and cases 10 or 11.

4.3.2. Changes in vortex fields in low KC_1/KC_2

Comparing the calculation results of cases 8, 9 and 10, it is easy to note that the vortices intensity caused by vibration in cases 9 and 10 is small, and it is not easy to cause significant changes in the wave vortex fields before the time of $\omega t = 360^\circ$. Compared with case 8, case 9 has earlier asymmetric vortices in the wake vortices area, which is due to the larger vortices strength of their shedding vortices. At $\omega t = 360^\circ$ and $\omega t = 450^\circ$, it can be observed that with the change in the direction of pile movement, the vortices in the temporary wake area is elongated due to inertia, and then the vortices morphology is different. The vortex field development of case 10 is very similar to that of case 9, but the vortices more easily fall off the sidewall. As the vortex intensity of the shedding vortices increases, a symmetrical shedding vortices also begin to form in the area in front of the pile. At the same time, it can be noted that in this study, only a pair of vortices shed from the pile, and the direction of the stream has changed. After that, the reverse flow velocity prevents the vortices shed from diffusing downstream.

Figure 24 also shows that when the velocity direction turns to the positive X-axis direction in the next cycle, the swirl intensity of the vortices falling off before is significantly reduced until it enters the extinction band and is dissipated. As the breakaway vortices drift along the positive direction of the X-axis, due to the mutual interference of the Lee wake vortices, asymmetric vortices begin to appear in the wake vortices area at $\omega t = 720^\circ$.

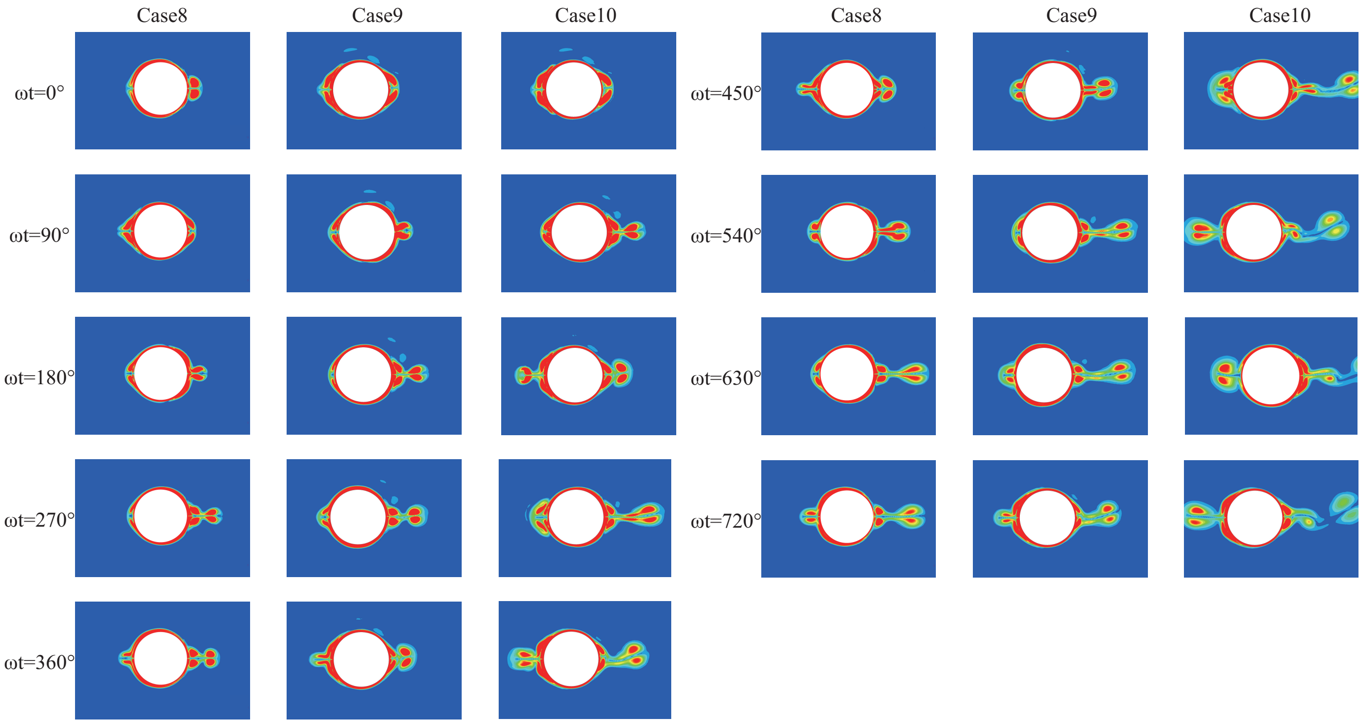

Figure 24. Vortex fields around piles of case 8, case9 and case10. After adding the pile vibration, the Lee wake vortices in front of the pile begin to appear, and the vortex fields are relatively messy. Therefore, the vortex fields section are taken at the position of $y = -0.3m$ for display.

4.3.3. Changes in vortex fields in high KC_1/KC_2

Figure 25 shows that the increase in pile amplitude causes considerable interference to the vortex fields. A particularly noteworthy phenomenon is that at 450°, a pair of vortices that has shed and interfered with each other to form an asymmetric structure have reattachment, which has a great impact on the symmetry of the vortex fields around the pile. This shows that at the next moment, asymmetric wall attached vortices immediately appeared on the sidewall of the pile. Then, as the pile moves away in the positive direction of the X-axis, the asymmetric wall attached vortices fall off the sidewall of the pile.

In case 12, with a further increase in amplitude, the pile vibration causes greater interference with the vortex fields. At $\omega t = 360°$, it is worth noting that a pair of convex shedding vortices appear at the positions of $\theta = 70°$, which are very similar to the tertiary vortices observed by Koumoutsakos in the pulse starting and braking pile flow. As the pile turns away, the vortices shift to the temporary wake region. The reattachment of asymmetric vortices in case 11 are clearer than those in case 12. At $\omega t = 630°$, a pair of vortices that have shed and interfered with each other to form an asymmetric structure have reattached. Similar to case 11, this reattachment has a great impact on the symmetry of the vortices on the pile surface. Fig.25 shows that at the next moment, asymmetric wall attached vortices immediately appear on the sidewall of the pile.

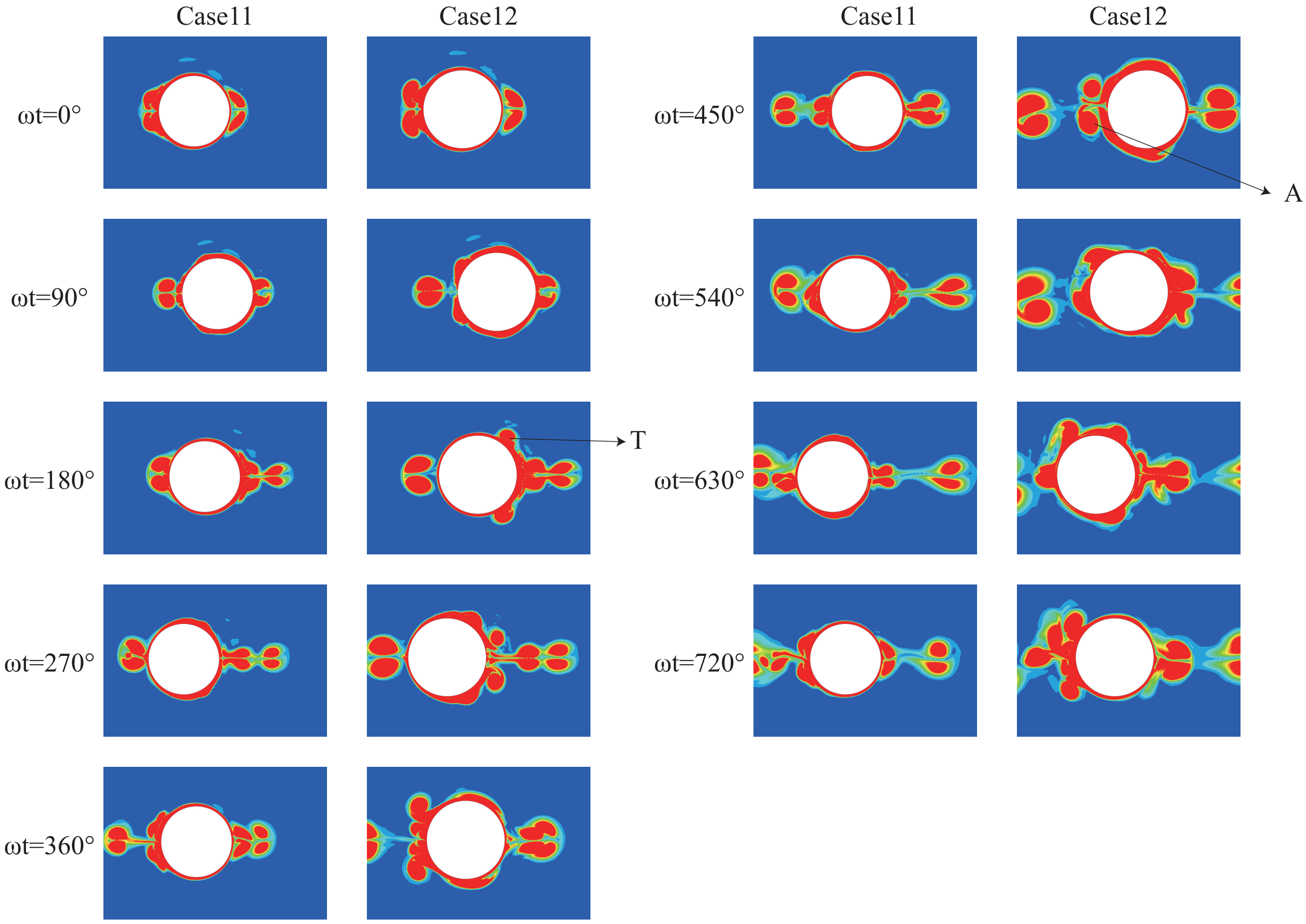

Figure 25. Vortex fields development process of case11 and case12. T is the shedding convex vortices, and A is the asymmetric separation vortices with reattachment.

4.3.4. Variation of vorticity on monopile surface

The vorticity distribution on the surface of the pile in a wave flume is much more complex than that in a calm water flume (Figure 26) . At such moments as $\omega t = 0°, 180°$ and 360°, upwelling and downwelling are dominant in the movement of wave water points, which mainly affect the formation of unformed horseshoe vortices at the bottom of the pile and make a small contribution to the sidewall vortices. The side shear flow caused by pile vibration is the main contributor to the sidewall vortices. In contrast, at the times of $\omega t = 90°$ and 270°, the horizontal flow is dominant in the wave water point motion, and the vibration of the pile is near the equilibrium position. At this time, the wave water point motion is the main contributor to the sidewall vortices. The figure shows that under the action of superposition, at $\omega t = 0°$, 180° and 360°, the vibration "pulls" the vorticity distribution to the distribution law of similar pile shear vorticity. At the same time, there are additional peaks in the temporary wake area, which reflects the emergence of additional high shear areas. At $\omega t = 90°$ and 270°, there are two additional peaks, corresponding to the backwards movement of the high shear zone and the additional high shear zone in front of the pile side. After the $\omega t = 360°$moment, the vorticity distribution of case 11 and case 12 shows obvious asymmetry,

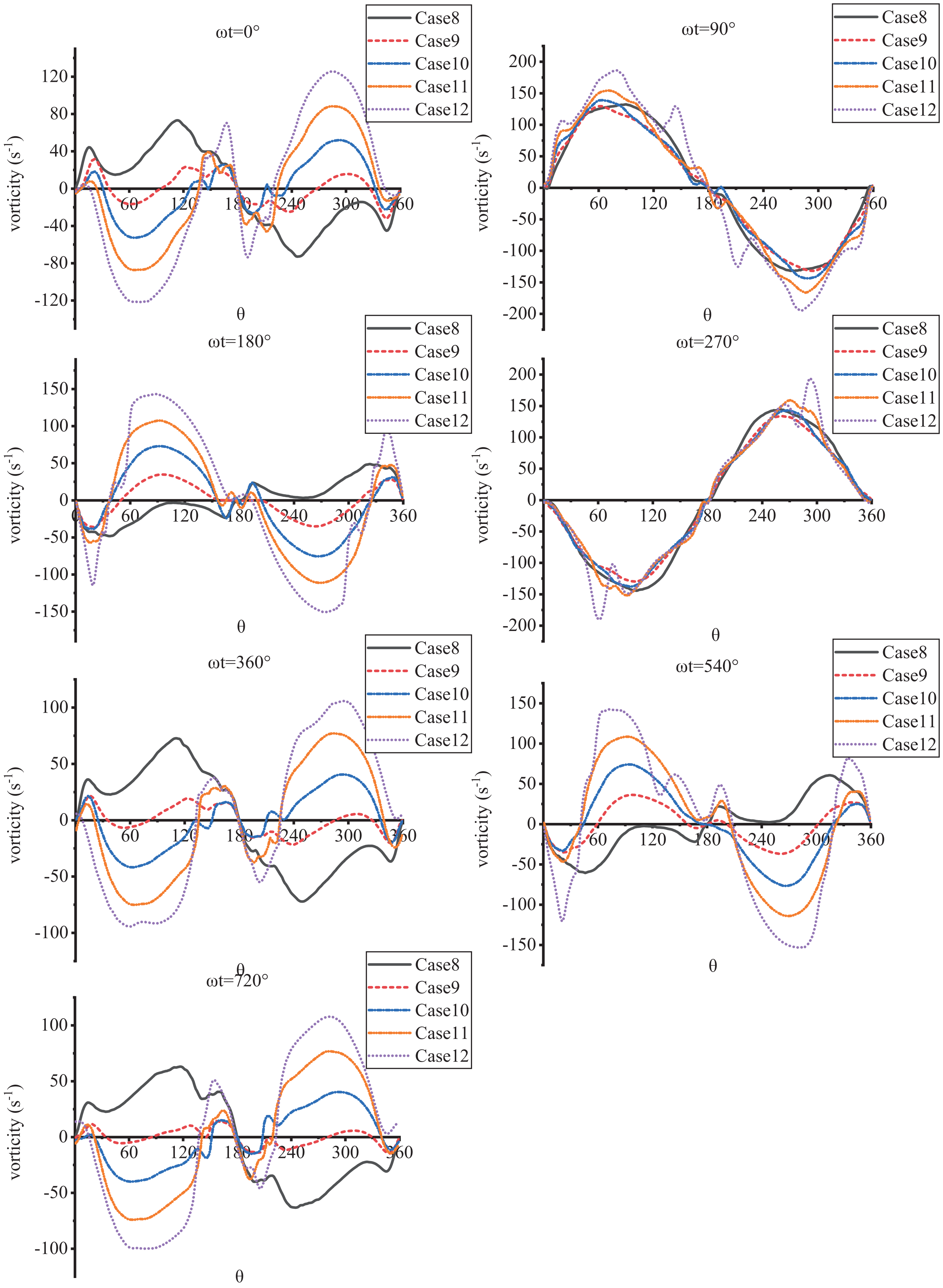

Figure 26. The vorticity distribution on the surface of the pile

4.3.5. Overall distribution of bed shear stress

Figure 27 shows the overall change in the shear stress around the pile for the 5 cases in the wave flume. In the shear flow region at the side of the pile, it can be noted that the high shear stress region appears in the area around the case 8 pile, which is caused by the horseshoe vortices upwelling/downwelling. Due to the insufficient backflow strength, the horseshoe vortices structures are not as stable as those in cases 4∼7, and the shear stress region also presents an irregular shape. It is worth noting that cases 9∼12 show great changes with increasing KC_1/KC_2 value. When the pile moves forward to the X-axis, under the action of inertia, the shear flow region moves to the rear side of the pile (Figure 28) . Accordingly, the high shear stress region at the side of the pile moves to the rear side of the pile. In case 11 and case 12, it is even fused with the shear stress region caused by the horseshoe vortices, which is difficult to distinguish.

With the movement of the pile, a high shear stress region is formed in the front area of the pile side, and the formation reason of this region is consistent with cases4∼7. Figure 28 also shows that under the superposition of wave and pile vibrations, two shear accelerated flow zones appear at the side of the pile.

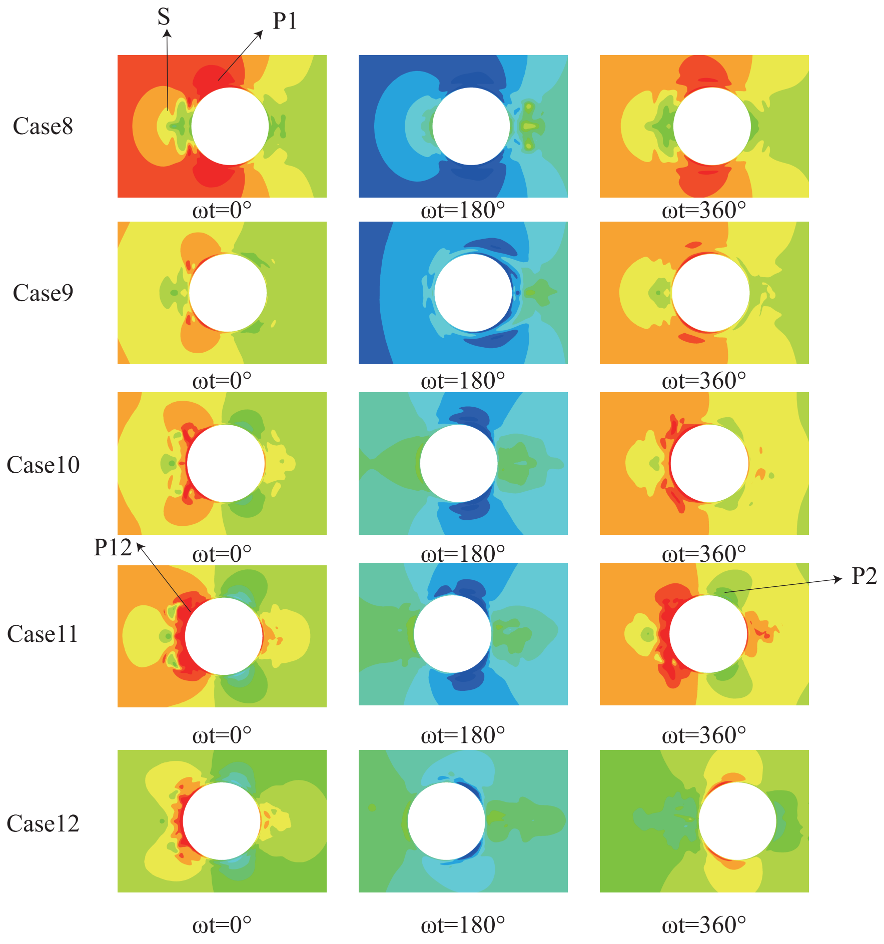

Figure 27. The overall distribution of shear stress around piles in case8∼12 . S is the high stress area caused by horseshoe vortices, P1 is the high stress area caused by wave shear flow, P2 is the high stress area caused by pile vibration shear flow, and P12 is the high stress area caused by wave shear flow moving backward under inertia

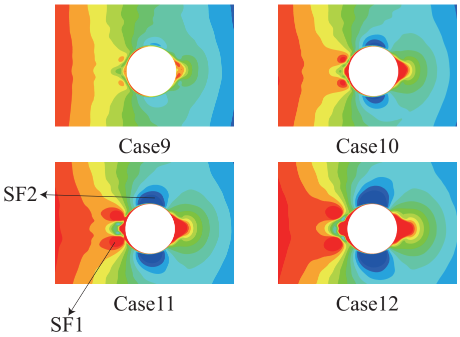

Figure 28. Velocity distribution around piles in case9∼case12. SF1 is the wave induced shear accelerated flow region with backward displacement, and SF2 is the additional shear accelerated flow region caused by vibration.

4.3.6. Phase Lead 557

Take the same measuring points as case3∼6 on the side of the pile column to monitor the time history of flow velocity and bed shear stress. Similar to the change of bed shear stress caused by pile vibration previously discussed, the change of bed shear stress time history curve here presents periodic characteristics. It is worth noting that compared with case3∼6, the peak of shear stress is no longer obvious, which reflects that waves play a leading role in the wave flume. Similar to the phenomenon in calm water, the phase leading angle originates from the upper edge of the boundary layer and develops towards the bed surface. Fig. shows that the phase lead angle decreases with the increase of KC_1/KC_2, which reflects the promotion of the disturbance of the pile to the turbulence development in the side area of the pile in the wave flume. Figure 29 and Figure 30 shows that the phase lead angles of case8 and 9 are close in value, and the same is true of case10 and 11, reflecting the sudden change of the influence of vibration on the phase lead angle. It is worth noting that the phase lead angle in case8 and 9 shows the feature that the offshore flow is greater than the onshore flow, while case8,9,10 is the opposite. This corresponds to the different results of Xie's wave flume test and van der's oscillating flow test[18,19]. It can be noted that there is no necessary value comparison relationship between the onshore and offshore phase lead angles.

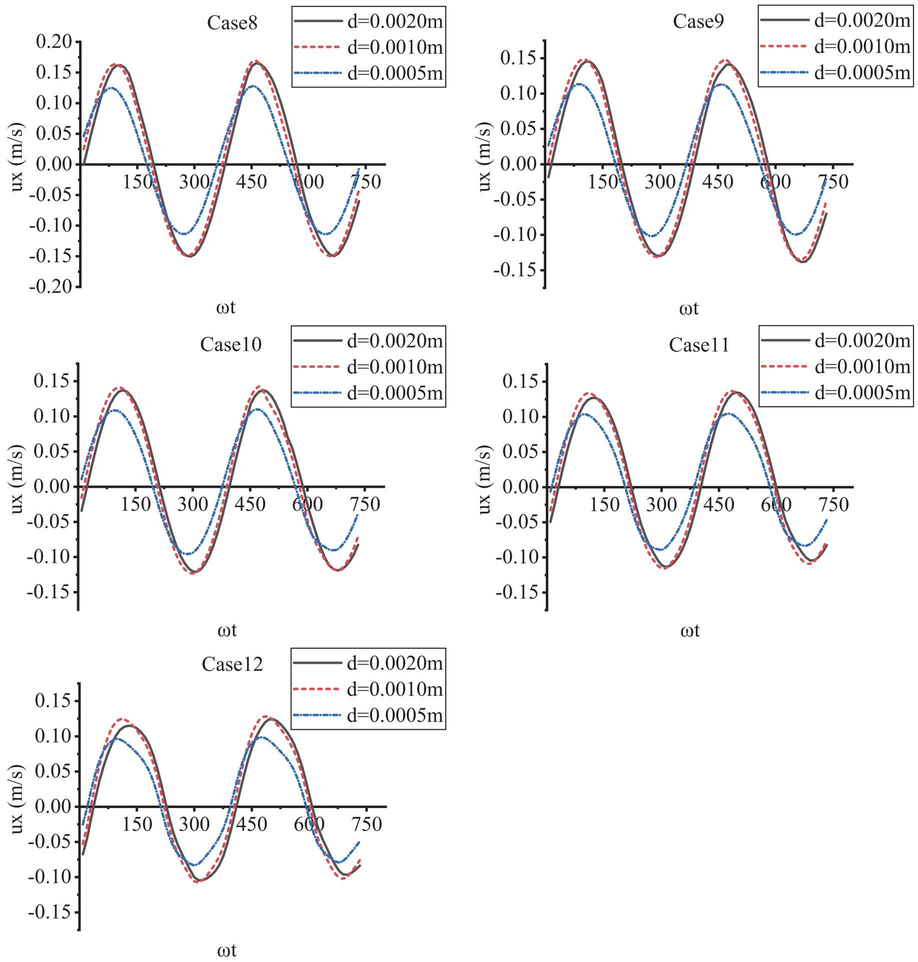

Figure 29. Phase lead effect in wave flume (boundary layer) .

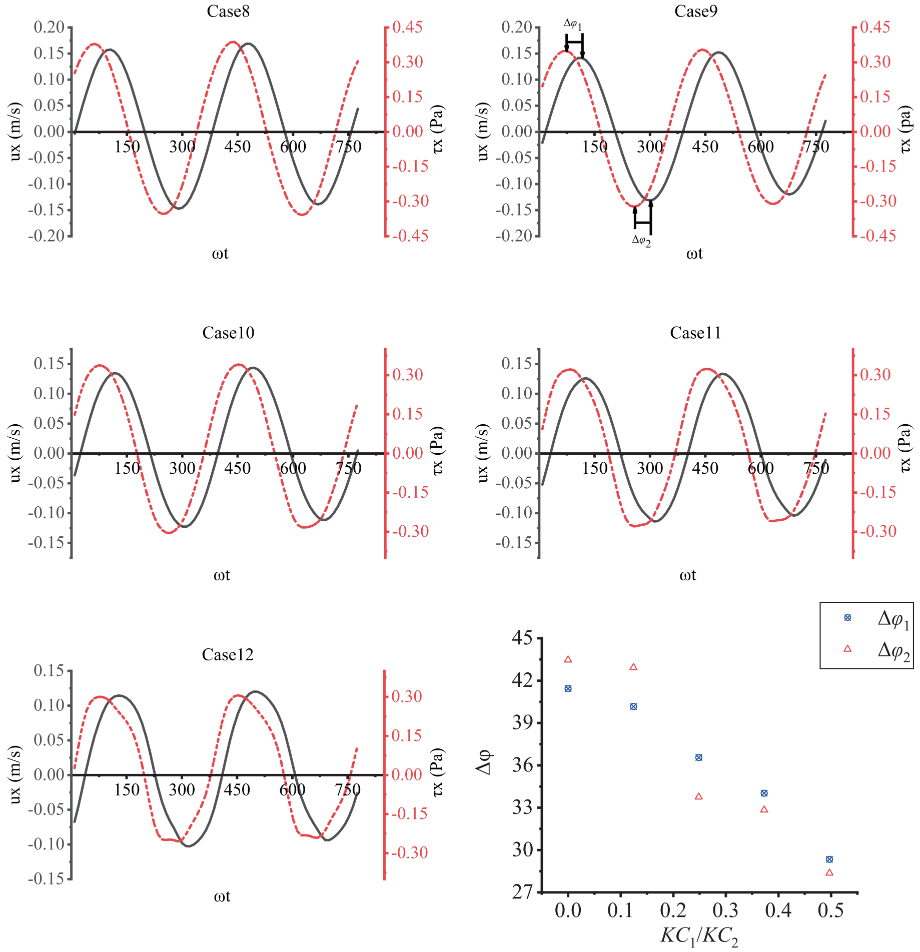

Figure 30. Phase lead effect in wave flume (bed shear stress) and phase angle.

4.3.7. Influence of vortices around monopile

Figure 31 shows that the shear stress value in front of the pile fluctuates violently, and the peak value of the stress value appears, which indicates the influence of the vortices in front of the pile on the shear stress. Figure 32 shows a horseshoe vortices system composed of several unformed horseshoe vortices in front of the pile. As mentioned above, upwelling/downwelling gradually plays a leading role in the process of changing the direction of flow velocity, and a horseshoe vortex structure is formed near the bottom of the pile. However, due to the insufficient backflow intensity, the horseshoe vortices are not fully developed, and a stable horseshoe vortex structure has not been formed in the whole flow process. The peak value of shear stress in the figure appears in $\omega t = 180°$ and $540°$, corresponding to the formation of vortices at the bottom of the pile at these moments in the figure.

Specifically, when downwelling is dominant (such as $\omega t = 180°$ and $\omega t = 540°$), the horseshoe vortices intensity increases and affects the bed surface, and the bed surface shear stress peaks. When positive and negative horizontal flow is dominant (such as $\omega t = 270°$), the main force of horseshoe vortices formation is the backflow of horizontal flow, and the strength of this backflow is less than that of downwelling, so the horseshoe vortices area decreases, the vortices strength decreases, and the influence on the bed shear stress decreases. When upwelling (such as $\omega t = 360°$) is dominant, the vortices intensity is further weakened, the vortices move up, and its influence on the shear stress is further weakened.

After the pile vibration is added, the peak value of the bed shear stress of case 9 is less obvious than that of case8. However, this is not because the influence of the vortices structures are weakened but rather from travel of the pile away from the measuring point during the vibration process. Figure 32 shows that the unformed horseshoe vortices appear within 5mm in front of the pile. When the pile is far from the measuring point, the influence of the horseshoe vortices are weakened. Even so, the figure still shows the difference in the change in the bed shear stress between the front and behind of the pile and the side of the pile. Obvious secondary peaks can be observed in the positive half cycle of the shear stress of cases 10∼12, and the secondary peak occurs when the pile approaches the measuring point. Figure 31 shows that vibration leads to an increase in the backflow intensity, the intensity of the horseshoe vortices also increases, and new vortices appear. Due to the increase in backflow strength, the shear stress increases significantly.

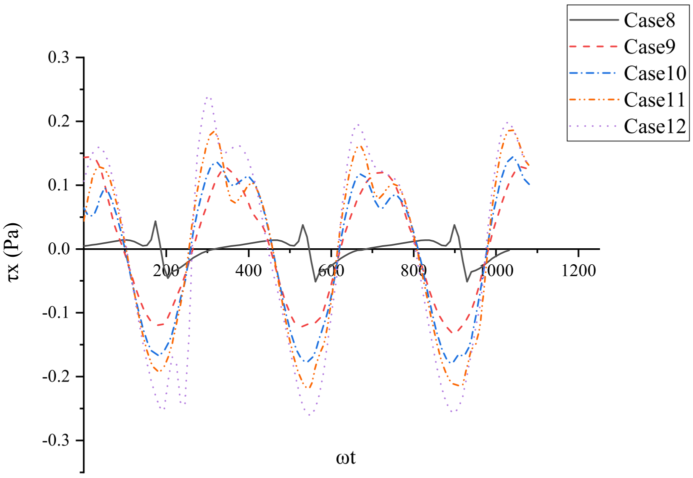

Figure 31. Time history of bed shear stress.

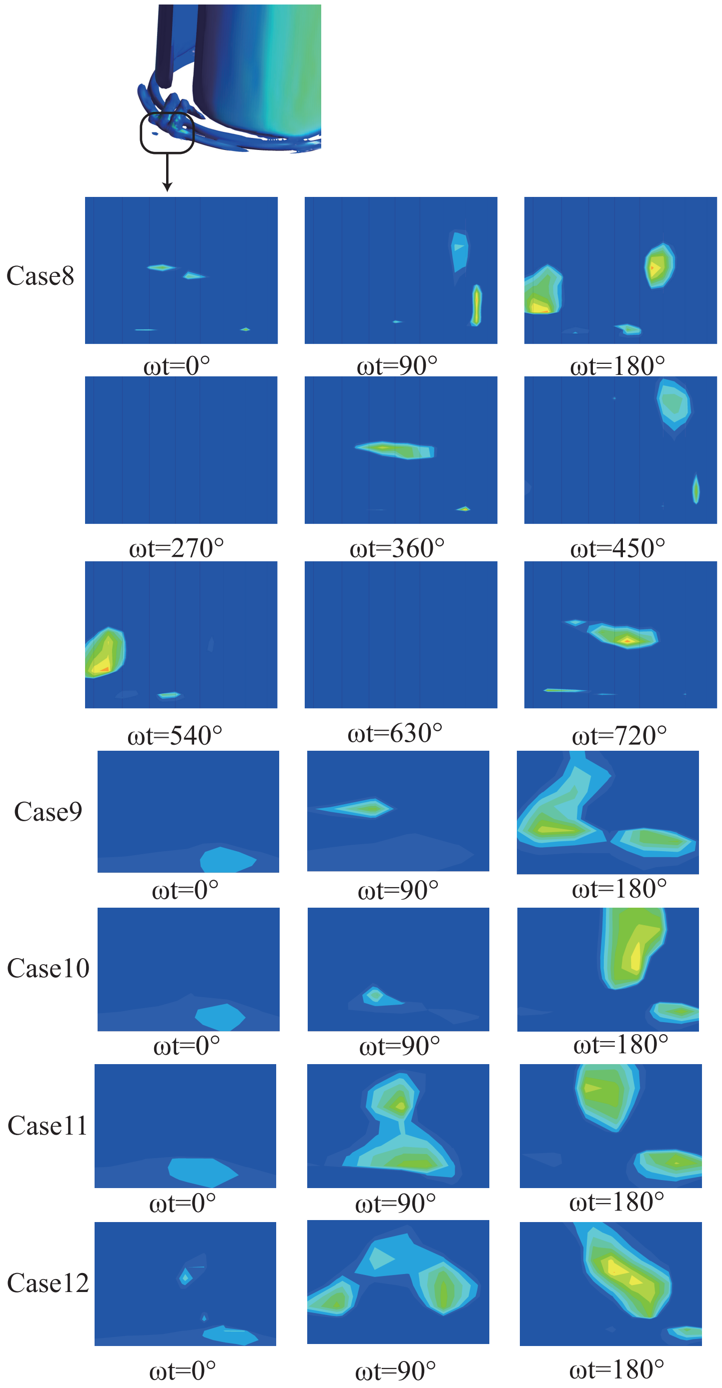

Figure 32. Horseshoe vortices system in Case8∼Case12.

5. Conclusions

In this study, the flow patterns around the pile in calm water and wave flume are discussed, and the changes of bed shear stress in the vortex fields around the pile are emphatically explored and summarized. The results show that the reattachment of shedding vortices is the main difference between the vortex fields of this study and that of static pile in calm water flume vortex fields and wave flume vortex fields; For the shear stress of the bed, the shear stress of the front and rear bed of the pile is mainly affected by vortices, and the shear stress of the side bed of the pile is mainly affected by shear accelerated flow.

The pile vibration affects the flow pattern around the pile in a disturbing way. The greater the vibration intensity, the stronger the disturbance of the pile to the flow field. An important effect of the increase of vibration intensity is that the shedding asymmetric vortices may reattach, and the reattachment phenomenon of vortices has a serious impact on the symmetry of the vortex fields on the side wall of the pile. If the separated asymmetric vortices reattach, the symmetry of the vortex fields on the side wall of the pile be destroyed, and the vortex fields become more chaotic and irregular in the subsequent cycle.

In the side area of the pile, the vibration of the pile makes the high stress area caused by wave shear flow moves back, and produce additional shear acceleration areas and high stress areas at the same time. In the front and behind of the pile-around flow field, the vibration of the pile leads to the increase of the backflow intensity, which leads to the increase of the horseshoe vortices intensity and the increase of the bed shear stress. In addition, under the influence of pile vibration, the phase lead effect of shear stress is obvious. In calm water flume and wave flume, the phase leading angle decrease with the increase of vibration intensity.

6. patents

Author Contributions: Conceptualization, Cheng YZ.; methodology, Shi YX.; investigation, Shi YX.; writing—original draft preparation, Shi YX.; writing—review and editing, Cheng YZ and Huang XY.; All authors have read and agreed to the published version of the manuscript.

Funding: This study was supported by the National Natural Science Foundation of China (Grant No. 52071031; 52171245), the Open Foundation of State Key Laboratory of Coastal and Offshore Engineering, Dalian University of Technology (Grant No. LP21V3), Project supported by the Research Foundation of Education Bureau of Hunan Province, China (Grant No.18B132). Postgraduate Research and Innovation Project of Changsha University of Science & Technology (Grant No. CX2021SS36).

Institutional Review Board Statement: Not applicable

Informed Consent Statement: Not applicable

Data Availability Statement: Not applicable

Acknowledgments: The authors thank Lu ML, Luo ZL and Liu YX for their help in wave making method, code, and numerical method. The authors also thank American Journal Experts and Edit Springs for their help in modification-Polish. The authors are grateful to the editors and anonymous reviewers for their helpful insights and comments throughout the review process.

References

1. MD Esteban, Offshore wind foundation design: some key issues.n. *Journal of Fluid Mechanics*. **2015**, *137(5)*, 051211.1–051211.6. https://doi.org/10.1115/1.4030316
2. Yagci, Clear water scour around a finite array of piles. *Applied Ocean Research*. **2017**, *68*, 114-129. https://doi.org/10.1016/j.apor.2017.08.014
3. AI Hammadi, Effect of vibration on the scour process around cylindrical structures under unidirectional flow in a sandy bed. *8th International Conference on Scour and Erosion*. **2016**, 157–161. https://doi.org/10.1201/9781315375045-20
4. Lee J, Unsteady flow of shear-thickening fluids around an impulsively moving circular pile. *Journal of Non-Newtonian Fluid Mechanics*. **2019**, *272*, 104163. https://doi.org/10.1016/j.jnnfm.2019.104163
5. Yun Y J, Unsteady flow of Carreau fluids around an impulsively moving pile. *Physics of Fluids*. **2020**, *32*, 123105. https://aip.scitation.org/doi/10.1063/5.0031431
6. Koumoutsakos, High-resolution simulations of the flow around an impulsively started pile using vortex methods. *J. Fluid Mech.* **1995**, *296(1)*, 1-38. https://doi.org/10.1017/S0022112095002059
7. Baykal C , Coutanceau M, Numerical simulation of scour and backfilling processes around a circular pile in waves. *Coastal Engineering*. **2017**,*122(APR.)*, 87-107. https://doi.org/10.1016/j.coastaleng.2017.01.004
8. Liu Y X , Coutanceau M,CFD investigation of blind-tee effects on flow mixing mechanism in subsea pipelines. *Engineering Applications of Computational Fluid Mechanics*.**2022**,*16(1)*, 1395-1419. https://doi.org/10.1080/19942060.2022.2093275
9. Hu R G , Scour Characteristics and Equilibrium Scour Depth Prediction around Umbrella Suction Anchor Foundation under Random Waves. *Journal of Marine Science and Engineering*.**2021**,*9(8)*, 886.

https://doi.org/10.1080/19942060.2022.2093275

10. A H Mirfenderesk, Direct measurements of the bottom friction factor beneath surface gravity waves. *Applied Ocean Research*.**2003**,*25(5)*, 269-287.
https://doi.org/10.1016/j.apor.2004.02.002
11. S.Carstensen, Fredsøe. Coherent structures in wave boundary layers. Part I. Oscillatory motion. *Journal of Fluid Mechanics*. **2010**, *646*, 169-206.
https://doi.org/10.1017/S0022112009992825
12. Yang P P, Effects of bed roughness on a horseshoe vortex in overland water flowing past a cylinder. *Journal of Hydrology*. **2022**,*606*, 127385.
https://https://doi.org/10.1016/j.jhydrol.2021.127385
13. Gazi A H, A review on hydrodynamics of horseshoe vortex at a vertical cylinder mounted on a flat bed and its implication to scour at a cylinder. *Acta Geophysica,*. **2020**, *68(3)*,861-875.
https://doi.org/10.1007/s11600-020-00439-8
14. Zhang W, Three-dimensional simulation of horseshoe vortex and local scour around a vertical cylinder using an unstructured finite-volume technique. *Transactions of Nanjing University of Aeronautics and Astronautics*. **2020**, *35(3)*, 12.
https://doi.org/10.1016/j.ijsrc.2019.09.001
15. Liang B C, Local Scour for Vertical Piles in Steady Currents: Review of Mechanisms, Influencing Factors and Empirical Equations. *Journal of Marine Science and Engineering*. **2020**, *8(1)*, 4.
https://doi.org/10.3390/jmse8010004
16. Sumer B M, A Tørum. Scour around coastal structures: a summary of recent research. *Coastal Eng*. **2001**, *44(2)*, 153-191.
https://doi.org/10.1016/S0378-3839(01)00024-2
17. Fredse J, Effect of externally generated turbulence on wave boundary layer. *Coastal Engineering*. **2003**, *49(3)*,153–183.
https://doi.org/10.1016/S0378-3839(03)00032-2
18. Van der, Experimental study of the turbulent boundary layer in acceleration-skewed oscillatory flow. *Journal of Fluid Mechanics*. **2011**, *684(10)*,251-283.
https://doi.org/10.1017/jfm.2011.300
19. Xie M X, Flow structure and bottom friction of the nonlinear turbulent boundary layer under stormy waves. *Coastal Engineering*. **2021**, *164*,103811.
https://doi.org/10.1016/j.coastaleng.2020.103811
20. Guan D W, Current-Induced Scour at Monopile Foundations Subjected to Lateral Vibrations. *Coastal Engineering*. **2018**, *164*,103811.
https://doi.org/10.1016/j.coastaleng.2018.10.011
21. Liu S, Influences of free surface jump conditions and different $k-\omega$ sst turbulence models on breaking wave modelling. *Ocean Engineering*. **2020**, *217*,107746.
https://doi.org/10.1016/j.oceaneng.2020.107746
22. Sami A M, Numerical and experimental analyses of the flow around a horizontal wall-mounted circular cylinder. *Transactions-Canadian Society for Mechanical Engineering*. **2009**, *33(2)*,189-215.
https://doi.org/10.1139/tcsme-2009-0017
23. Devolder B, Performance of a buoyancy-modified $k-\omega$ and $k-\omega$ sst turbulence model for simulating wave breaking under regular waves using openfoam. *Coastal Engineering*. **2009**, *138*,49-65.
https://doi.org/10.1016/j.coastaleng.2018.04.011
24. Menter F, Zonal two equation $k-\omega$ turbulence models for aerodynamic flows. *24th Fluid Dynamics Conference*. **1993**, *229*,1-21.
https://doi.org/10.2514/6.1993-2906
25. Liu Z J, An improved local correlation-based intermittency transition model appropriate for high-speed flow heat transfer. *Aerospace Science and Technology*. **2020**, *106*,106122.
https://doi.org/10.1016/j.ast.2020.106122
26. Jensen B L, Turbulent oscillatory boundary layers at high reynolds numbers. *J. Fluid Mech*. **1989**, *206*, 265-297.
https://doi.org/10.1017/S0022112089002302
27. Liu C Q, New omega vortex identification method. *SCIENCE CHINA Physics, Mechanics and Astronomy*. **2016**, *8*, 9.
https://doi.org/10.1007/s11433-016-0022-6
28. Liu C Q, Third generation of vortex identification methods: omega and liutex/rortex based systems. *SCIENCE CHINA Physics*. **2019**, *31(2)*, 19.
https://doi.org/10.1007/s42241-019-0022-4